Astronomy & Astrophysics manuscript no. MS29813˙final
November 28, 2016

Kinematics of the Local Universe XIV.

Measurements from the 21 cm line and the HI mass function from a homogeneous catalog gathered with the Nançay radio telescope

G. Theureau[1,2,3], N. Coudreau[3], N. Hallet[3], M. 0. Hanski[1,5], and M. Poulain[1]

[1] LPC2E, CNRS, Univ. Orléans, F45071 Orleans Cedex 02, France
[2] Station de Radioastronomie de Nançay, Observatoire de Paris, PSL Research University, CNRS, Univ. Orléans, F18330 Nançay, France
[3] LUTh, Observatoire de Paris, PSL Research University, CNRS, F92195 Meudon Principal Cedex, France
[4] GEPI, Observatoire de Paris, PSL Research University, CNRS, F92195 Meudon Principal Cedex, France
[5] Tuorla observatory, University of Turku, SF 21500 Piikkiö, Finland

Received : 2016 September 30 / accepted : 2016 November 4

ABSTRACT

Aims. This paper presents 828 new 21 cm neutral hydrogen line measurements carried out with the FORT receiver of the meridian transit Nançay radio telescope (NRT) in the years 2000 – 2007.
Methods. This observational program was part of a larger project aimed at collecting an exhaustive and magnitude-complete HI extragalactic catalog for Tully-Fisher applications. Through five massive data releases, the KLUN series has collected a homogeneous sample of 4876 HI-spectra of spiral galaxies, complete down to a flux of 5 Jy.km.s^{-1} and with declination $\delta > -40°$.
Results. We publish here the last release of the KLUN HI observational program, corresponding to the faint end of the survey, with HI masses ranging from 5 10^8 to 5 10^{10} solar masses. The size of this final sample is comparable to the catalogs based on the Arecibo and Parkes radio telescope campaigns, and it allows general HI mass distribution studies from a set of homogeneous radio measurements.

Key words. Astronomical data bases: miscellaneous – Surveys – Radio lines: galaxies

1. Introduction

The present paper is the last in a long series of extragalactic HI spectra releases obtained from the long-term EDS [1] and KLUN[2] surveys at the Nançay radio telescope. We publish here a collection of new HI line measurements of spiral galaxies, complementing previous publications by Bottinelli et al. (1992), Bottinelli et al. (1993) (EDS), di Nella et al. (1996), Theureau et al. (1998a), Paturel et al. (2003b), Theureau et al. (2005), and Theureau et al. (2007) (KLUN). The KLUN program has received the label of key project of the refurbished instrument (FORT receiver) and was allocated an average of 20 % of the observing time from mid 2000 to late 2006.

This survey is complementary to other large HI projects led in the 2000s, such as the blind surveys HIPASS[3] with the Parkes radio telescope (Meyer et al. 2004) and ALFALFA with the Arecibo radio telescope (Haynes et al. 2011), or the Arecibo HI data compilation by Springob et al. (2005). In the last period of the survey corresponding to the present publication, the majority of the galaxies were observed from Nançay in the range (-40°,+0°) in declination, favoring the declination range unreachable by Arecibo. Furthermore, our aim was to fill the gaps left in the last Hyperleda HI compilation by Paturel et al. (2003b) in order to reach well-defined selection criteria in terms of redshift coverage and magnitude completeness for Tully-Fisher applications. The input catalog has been put together from a compilation of the Hyperleda extragalactic database completed by the 2.7 million galaxy catalog extracted from the DSS (Paturel et al. (2003a)), and the releases of the DEep Near Infrared Survey (DENIS; Paturel et al. 2005) and the 2 Micron All Sky Survey (2MASS; Jarrett et al. 2000) near-infrared (NIR) CCD surveys. All targeted objects were inspected by eye on optical and/or NIR images, to select only late-type galaxies, from Sa to Sm morphologies.

The total Nançay HI catalog used for the KLUN analysis contains 4876 spiral galaxies, whose 21 cm line spectra were acquired across two receiver generations, and processed with a homogeneous reduction and calibration pipeline, all along the total observation campaign, from 1992 to 2006 (see in particular Theureau et al. (1998a) and Theureau et al. (2005) for details). This HI catalog is comparable in size with the Parkes and Arecibo catalogs, which were made public around 2005, and allows the same kind of general statistical HI mass studies as published respectively by Zwaan et al. (2005) and Springob et al. (2005). We thus complement the data publication with a few results in terms of HI mass and its variation with galaxy morphology.

The present paper is structured in two main sections. The Nançay radio telescope (NRT), the processing chain,

[1] Extragalactic Distance Scale
[2] for Kinematics in the Local UNiverse
[3] http://www.atnf.csiro.au/research/multibeam/release/

Table 1. Statistics of the detected galaxies vs. HI profile class.

profile class	no. of gal.	no. of HI confusions
A	160	11
B	303	34
C	174	46
D	86	5
E	104	3

the reduced HI data[4], and the general properties of the catalog are presented in Section 2; we repeat there the main characteristics of the instrument and of the data, which were described more extensively in Theureau et al. (2005). Section 3 shows an example of HI mass function analysis, together with elements of comparison with previous extensive results by Springob et al. (2005), Zwaan et al. (2005), and Haynes et al. (2011).

2. HI campaign

2.1. Sample characteristics

As a last KLUN HI data release, we present here 21 cm line measurements obtained for 828 targeted galaxies, observed between mid 2000 and late 2006, the majority of which were close to the limit of detection. With this publication, the total contribution of the so-called KLUN program to the HI spectra budget amounts to 4876 galaxies, collected over a period of $\sim$ 15 years, with a homogeneous data reduction pipeline. This composite HI sample was built by gathering the data from the five publications of the KLUN series: Theureau et al. (1998a), Paturel et al. (2003b), Theureau et al. (2005), Theureau et al. (2007), and this paper.

Figure 1 shows the general statistics of the Nançay HI catalog for both the total KLUN composite sample and the subpart of 828 new measurements presented in this paper. As mentioned above, the vast majority of the targets were chosen outside the Arecibo field, between the Nançay declination lower limit -40° and the Arecibo threshold at -1°. Most of the observed galaxies are in the range 4 000-10 000 km.s^{-1}, where the lack of Tully-Fisher measurements in the literature was the most critical. Since this publication presents the epilog of the KLUN observational program, a large number of the HI spectra released here are from faint HI galaxies, close to the limit of detection (with HI-line S/N often below 5) and which often required several hours of exposure time to get measurable line parameters. The NRT is a quasi-meridian instrument, with a maximum one-hour daily window at a given RA, which means that the observations of a given galaxy were systematically scheduled to spread over several transits, sometimes separated by months. Actually, the integration time per galaxy and per polarization spans from 15 minutes (e.g., pgc36297) to 6 hours (e.g., pgc4566), with an average value around 2 hours. The final spectrum is obtained by summing the two banks in vertical and horizontal polarizations and applying a boxcar smoothing to get the final resolution of typically $\sim$10 km.s^{-1} at 21 cm. During the period covered by the survey, the evolving S/N was checked after each transit and a given target was classified as "completed" only once it reached S/N $\geq$ 5, or if we reached a rms noise smaller than 2 mJy, which is a reasonable detection threshold for the instrument. For these faint objects it was generally the latter case, since most of the high S/N HI galaxy spectra were published in the previous KLUN releases.

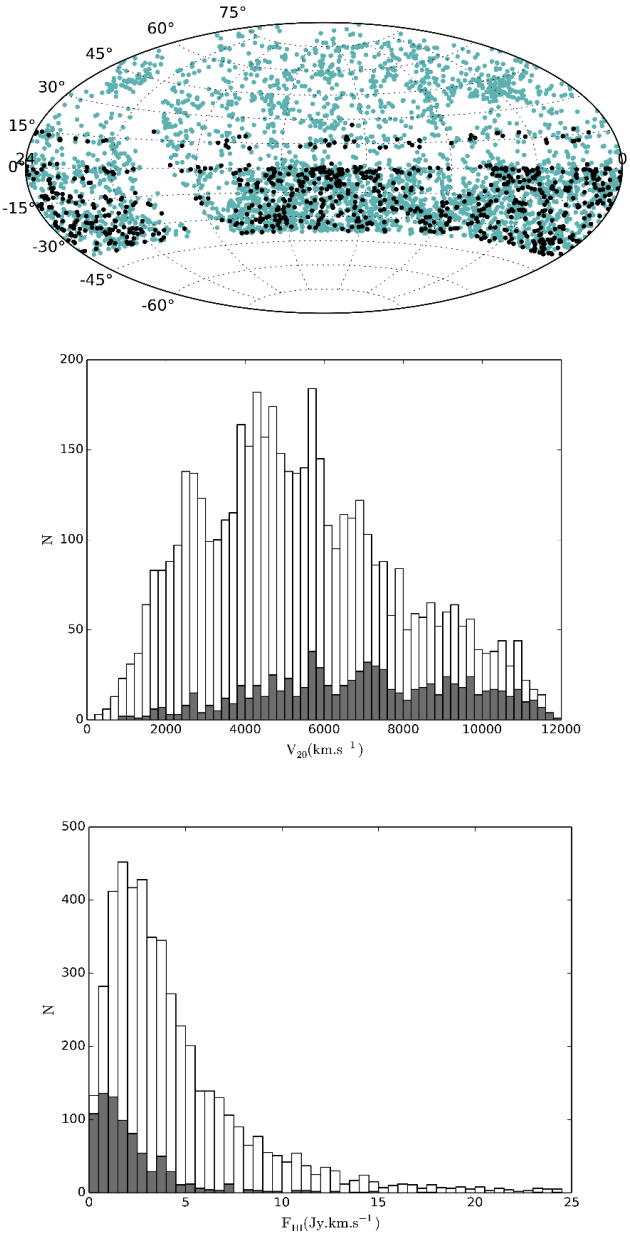

Fig. 1. General statistics of the KLUN HI catalog. Top : Aitoff projection of the KLUN composite Nançay HI-data catalog (cyan dots: Theureau et al. (1998a), Paturel et al. (2003b), Theureau et al. (2005), Theureau et al. (2007); black dots: the galaxies added in this publication). Middle: distribution of radial velocities (optical convention) for the KLUN composite catalog (white columns) and this paper (gray columns). Bottom: distribution of beam-corrected HI-fluxes (same samples).

[4] Tables 2 and 3, together with HI profiles in ASCII format are available via anonymous ftp to cdsarc.u-strasbg.fr (130.79.128.5) or via http://cdsweb.u-strasbg.fr/cgi-bin/qcat?J/A+A/

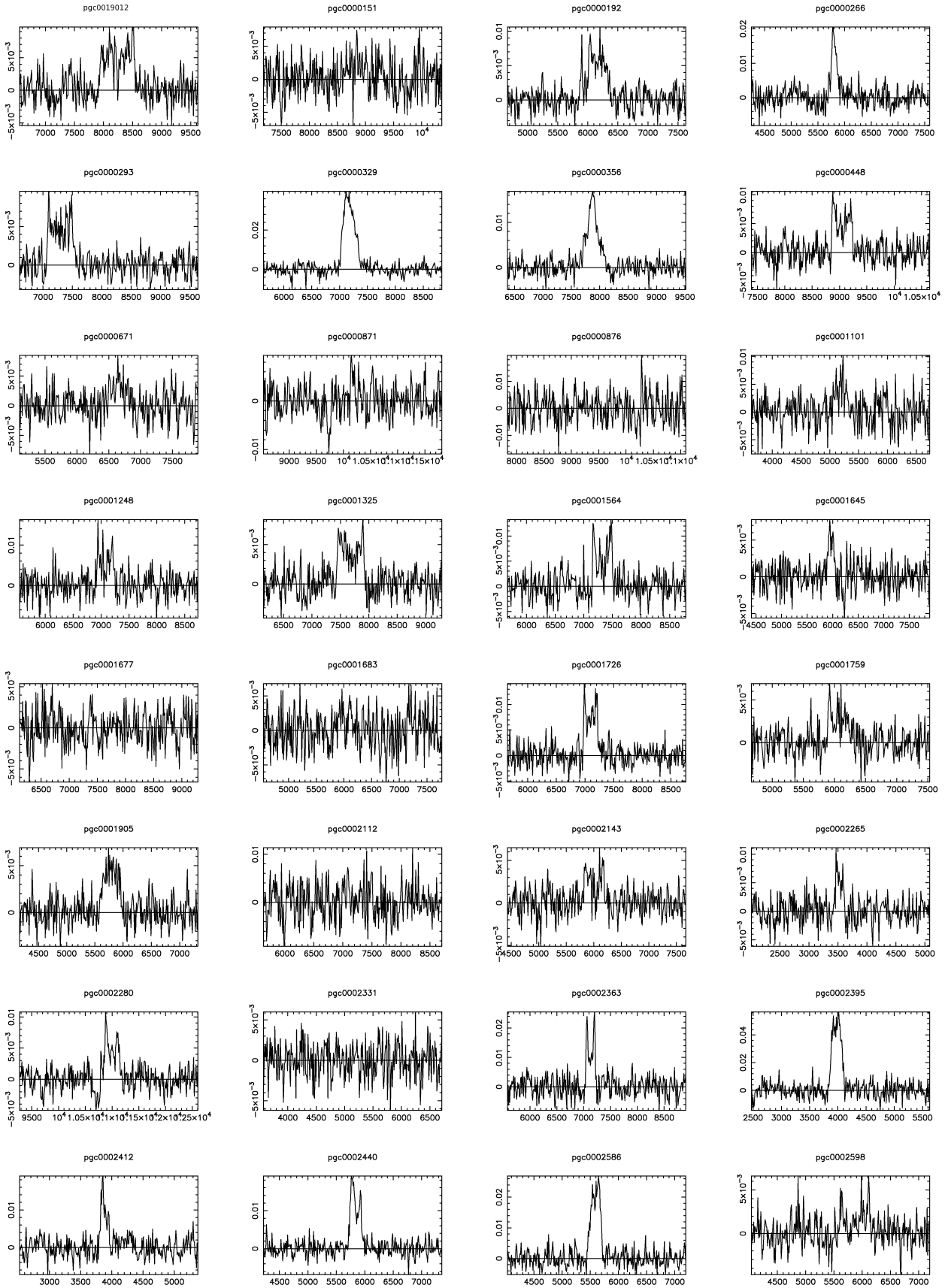

Fig. 2. -excerpt. 21 cm line profiles of galaxies listed in Table 2. The profiles are classified according to their PGC name which is written above each panel. Ordinate and abscissae axes are graduated respectively in km s^{-1} and Jy. The heliocentric radial velocities are expressed in terms of optical redshift $c\frac{\Delta\lambda}{\lambda}$. The horizontal line represents the baseline of the profile, i.e. the zero flux level, from which the maximum is estimated. Figure 2 continues in appendix A1.

pgc/leda	NAME	RA (2000) DEC	V_{20}	σ_V	W_{20}	W_{20c}	σ_{W20}	W_{50}	W_{50c}	σ_{W50}	F(HI)	F(HI)$_c$	σ_F	S/N	rms	Q
pgc0019012	2MASJ06252	J062529.4-321701	8076.0	24.0	314.0	260.0	73.0	289.0	261.0	49.0	1.31		0.74	2.0	2.7	B?
pgc0000151	ESO349-020	J000203.9-332802													2.8	E
pgc0000192	PGC000192	J000248.6-033622	6176.0	22.0	381.0	327.0	65.0	318.0	290.0	43.0	1.98	1.98	0.54	3.6	1.7	Cc
pgc0000266	PGC000266	J000345.1-144140	5815.0	12.0	175.0	128.0	37.0	109.0	88.0	25.0	2.14		0.52	6.5	2.7	B
pgc0000293	PGC000293	J000412.1-143125	7307.0	17.0	478.0	424.0	51.0	430.0	401.0	34.0	2.22	2.28	0.49	4.0	1.4	B
pgc0000329	PGC000329	J000447.2-013413	7182.0	5.0	323.0	269.0	15.0	280.0	252.0	10.0	8.51	8.56	0.72	13.3	2.6	C?
pgc0000356	PGC000356	J000507.6-034822	7884.0	15.0	357.0	303.0	44.0	169.0	142.0	29.0	3.28	3.3	0.42	9.2	1.6	Cc
pgc0000448	ESO409-018	J000604.1-303743	9047.0	9.0	382.0	328.0	26.0	373.0	344.0	17.0	2.06	2.12	0.6	3.5	2.0	A
pgc0000671	ESO349-034	J000924.4-364258	6613.0	14.0	243.0	190.0	41.0	237.0	208.0	27.0	0.8	0.8	0.6	1.8	2.6	D
pgc0000871	PGC000871	J001301.9-131526	10261.0	33.0	275.0	221.0	98.0	253.0	224.0	65.0	0.6	0.6	0.65	1.4	3.2	D
pgc0000876	PGC000876	J001303.4-304314													5.8	E
pgc0001101	PGC001101	J001641.5-103311	5186.0	21.0	274.0	220.0	62.0	250.0	221.0	41.0	1.06	1.07	0.62	2.3	2.7	D
pgc0001248	PGC001248	J001920.8-105639	7073.0	21.0	345.0	291.0	62.0	297.0	268.0	41.0	1.94	1.97	0.73	3.3	2.9	B
pgc0001325	ESO473-016	J002042.1-231658	7681.0	15.0	489.0	435.0	45.0	463.0	435.0	30.0	1.98	2.04	0.56	3.3	1.7	B
pgc0001564	PGC001564	J002518.3-143327	7327.0	7.0	349.0	295.0	22.0	339.0	310.0	15.0	2.11	2.14	0.61	4.2	2.4	A
pgc0001645	PGC001645	J002638.3-303301	5971.0	13.0	164.0	118.0	40.0	148.0	122.0	27.0	0.67	0.68	0.35	3.0	1.8	A
pgc0001677	PGC001677	J002714.6-074713													2.2	E
pgc0001683	PGC001683	J002720.0-045329													2.8	E
pgc0001726	PGC001726	J002802.4-080716	7101.0	8.0	263.0	209.0	25.0	242.0	214.0	16.0	2.05	2.05	0.48	5.4	2.0	A?
pgc0001759	IC0018	J002835.0-113512	5986.0	12.0	195.0	145.0	35.0	184.0	156.0	24.0	0.58	0.59	0.33	2.8	1.7	C?
pgc0001905	IC0025	J003112.1-002426	5773.0	18.0	375.0	321.0	55.0	345.0	317.0	37.0	1.42	1.42	0.46	2.9	1.4	B
pgc0002112	ESO294-023	J003513.1-373329													3.7	E
pgc0002143	NGC0166	J003548.8-133638	6007.0	14.0	371.0	317.0	41.0	362.0	333.0	27.0	0.93	0.95	0.44	2.2	1.5	C
pgc0002265	ESO411-002	J003755.2-285523	3530.0	14.0	170.0	123.0	41.0	147.0	121.0	27.0	0.85	0.87	0.4	3.5	2.1	B
pgc0002280	PGC002280	J003818.4-145056	10983.0	19.0	383.0	329.0	57.0	349.0	320.0	38.0	1.68	1.68	0.54	3.0	1.7	C?
pgc0002331	NGC0191	J003859.4-090010													2.2	E
pgc0002363	ESO411-004	J003918.8-295644	7130.0	5.0	182.0	134.0	15.0	170.0	143.0	10.0	2.42	2.45	0.59	6.9	3.2	A
pgc0002395	NGC0207	J003940.7-141414	3982.0	8.0	253.0	200.0	24.0	208.0	179.0	16.0	9.69	9.75	1.39	8.2	5.3	A?
pgc0002412	PGC002412	J004005.6-200349	3876.0	10.0	165.0	119.0	30.0	136.0	111.0	20.0	1.52	1.54	0.47	5.4	2.5	B
pgc0002440	IC1571	J004037.9-001950	5836.0	7.0	241.0	188.0	21.0	200.0	172.0	14.0	2.81	2.87	0.43	9.0	1.9	A?
pgc0002586	PGC002586	J004317.7-063834	5583.0	7.0	250.0	197.0	21.0	212.0	183.0	14.0	4.3	4.32	0.62	8.7	2.5	A?
pgc0002598	PGC002598	J004328.5-062055	5860.0	36.0	574.0	520.0	107.0	536.0	507.0	71.0	0.94	0.94	0.52	1.7	1.6	D
...	...	...	...	...	...	...	...	...	...	...	...	...	...	...	...	...

Table 2. -excerpt. Astrophysical HI-parameters (first 32 galaxies corresponding to Fig. 2).
Column 1: PGC or LEDA galaxy name;
Column 2: most usual galaxy name;
Column 3: J2000 equatorial coordinates;
Column 4: systemic heliocentric radial velocity (km s^{-1});
Column 5: rms error (km s^{-1});
Column 6: total line width at 20% of the maximum intensity (km s^{-1});
Column 7: total corrected line width at 20% (km s^{-1});
Column 8: rms error (km s^{-1});
Column 9: total line width at 50% of the maximum intensity (km s^{-1});
Column 10: total corrected line width at 50% (km s^{-1});
Column 11: rms error (km s^{-1});
Column 12: observed HI-flux (Jy km s^{-1});
Column 13: beam-filling corrected HI-flux (Jy km s^{-1});
Column 14: rms error (Jy km s^{-1});
Column 15: signal-to-noise ratio;
Column 16: rms noise;
Column 17: quality code (2.2) ; flag ("c" indicates confirmed HI confusion with the emission of another galaxy; "?" means that confusion is suspected but not certain).

2.2. Measured HI parameters

The NRT design, characteristics of the FORT receiver, spectrograph, and data pipeline were exhaustively described in Theureau et al. (2005).

Here we only describe the corrections applied to the raw measurements of the HI-line to get the parameters of astrophysical interest. An excerpt of the catalog of HI-astrophysical parameters, of observers' comments, and plots of the 21 cm line spectra is given respectively in Table 2, Table 3, and Fig 2. The full sample is available in electronic format at the CDS[4].

Spectrum quality code and HI confusion check. Table 2 contains all the reduced HI parameters. The local environment and possible HI confusion within the source beam or off beam has been checked by eye on the basis of online DSS and SDSS images and available astrophysical data from the Hyperleda and NED extragalactic data bases. Table 3 provides corresponding comments, when necessary, for each

pgc/leda	Q	Type	comments
pgc0019012	B?	Sa	=ESO426-007=2MASXJ06252935-3217012 poss HI confusion w pgc3081242 in off beam V=8284
pgc0000151	E	Sa	=ESO349-020 V=8760
pgc0000192	Cc	Sc	HI confusion w pgc0000176 3 arcmin N-NW V=6465 Sbc and pgc0000183 3 arcmin W, V=6290 prob late-type
pgc0000266	B	Sc	
pgc0000293	B	Sc	
pgc0000329	C?	Sab	poss HI confusion w pgc0000330 4 arcmin N V=7110 and pgc0000352 1 arcmin S-SE, V=7187 both prob late-type
pgc0000356	Cc	Sc	HI confusion w pgc169982 3 arcmin SW V=7851 face-on
pgc0000448	A	Sab	
pgc0000671	D	Sc	=ESO349-034
pgc0000871	D	S0-a	V=10330
pgc0000876	E	S0-a	V=9320, pgc0713877 in beam w V=9500
pgc0001101	D	S0-a	V=5196
pgc0001248	B	Sab	
pgc0001325	B	Sa	=ESO473-016
pgc0001564	A	Sc	
pgc0001645	A	Sa	
pgc0001677	E	S0-a	V=6728 cataloged as late-type in Huchra et al. 2012 ApJS 199, 26
pgc0001683	E	Sc	V=6123
pgc0001726	A?	Irr?	V=116 in Lavaux & Hudson 2011 MNRAS 416, 2840; poss HI confusion w pgc172103, 6 arcmin SW V=7217
pgc0001759	C?	Sb	=IC0018, merger ? poss HI confusion w pgc138190 in off beam V=6075 and w IC0019, 3.5 arcmin S V=6177
pgc0001905	B	Sab	=IC0025
pgc0002112	E	Sa	=ESO294-023 V=7242
pgc0002143	C	Sa	=NGC166
pgc0002265	B	Sc	=ESO411-002
pgc0002280	C?	Sab	poss HI confusion w group of 2MASS gal in off beam at J003645.8-145953 no V
pgc0002331	E	Sc	=NGC0191 V=6076
pgc0002363	A	Sc	=ESO411-004
pgc0002395	A?	Sa	=NGC0207, pgc138206 3.5 arcmin N V=3959, prob early-type, confusion ?
pgc0002412	B	Sc	
pgc0002440	A?	Sb	=IC1571, poss HI confusion w nearby group within 4 arcmin and ¡V¿=5800
pgc0002586	A?	Sc	poss HI confusion w pgc2583 1.5 arcmin S no V Sm
pgc0002598	D	S0	low S/N
...	...	...	...

Table 3. -excerpt. Notes on HI-observations (first 32 galaxies corresponding to Fig. 2).
Column 1: PGC or LEDA galaxy name;
Column 2: quality code and HI-confusion flag "c" (confirmed) or "?" (possible);
Column 3: comments; comp=companion, cf=comparison field, poss=possible, w=with, prob=probable.

galaxy. Comments mainly concern object designation, peculiar morphology, peculiar HI line shape, spectrum quality, or HI confusion. The spectra and extracted data are assigned a quality code from A to E, with decreasing spectrum quality (see Theureau et al. (2005) for details). In short, A and B classes correspond to well-defined HI profiles and subsequent measured HI parameters, while in classes C and D only the radial velocity is reliable owing to disrupted baseline and/or a signal-to-noise ratio (S/N) that is too low, and E stands for non-detection. In addition, a flag of "?" or "c" indicates suspected or confirmed HI line confusion. The distribution of the targets among the different classes is summarized in Table 1, together with the respective number of HI confusion.

Radial velocities. Our observed radial velocities are listed in Table 2 (column 4) and correspond to the median point of the 21 cm line profile measured at 20% of maximum intensity. The internal mean error on V_{20} is calculated according to Fouque et al. (1990) as

$$\sigma(V_{20}) = \frac{4 \cdot (R \cdot \alpha)^{1/2}}{S/N},$$

where R is the actual spectral resolution, $\alpha = (W_{20} - W_{50})/2$ is the slope of the line profile, and S/N is the signal-to-noise ratio. The average of $\sigma(V_{20})$ is about 8 km.s^{-1}. The radial velocity distribution of the sample is shown in Fig. 1 and is compared with the whole Nançay KLUN catalog.

Line widths are measured on the observed profile at two standard levels corresponding to 20% and 50% of the maximum intensity of the line. The results listed in Table 2, columns 6 and 9, have been corrected to the optical velocity scale. We also provide line widths corrected for resolution effect (Fouque et al. (1990)) in columns 7 and 10. The mean measurement error is taken equal to $3 \cdot \sigma(V_{20})$ and $2 \cdot \sigma(V_{20})$ for the 20% and 50% widths, respectively. The data presented here are not corrected for internal velocity dispersion. Details about these corrections can be found in

Bottinelli et al. (1990), Fouque et al. (1990), or Paturel et al. (2003b).

HI-fluxes are calibrated using as templates a set of well-defined radio continuum sources observed each month and further checked with a sample of "typical" galaxies observed regularly during the survey period and reduced through the same pipeline. Again, the detailed description of the flux calibration is given in Theureau et al. (2005). HI-fluxes F_{HI} (Table 2, column 12) are expressed in Jy km.s^{-1}. The values given in column 13 are corrected for beam-filling according to Paturel et al. (2003b)

$$F_{HIc} = B_f \cdot F_{HI},$$

where F_{HI} is the observed raw HI-flux,

$$B_f = \sqrt{(1+xT)(1+xt)},$$

$$T = (a_{25}^2 \sin^2\beta + b_{25}^2 \cos^2\beta)/\theta_{EW}^2,$$

$$t = (a_{25}^2 \cos^2\beta + b_{25}^2 \sin^2\beta)/\theta_{NS}^2,$$

θ_{EW} and θ_{NS} are the half-power beam dimensions of the Nançay antenna, β is the position angle of the galaxy defined northeastwards, and a_{25} and b_{25} are respectively the photometric major and minor axis. The parameter x is $x = 0.72 \pm 0.06$ (Bottinelli et al. 1990). Finally, owing to the Kraus design of the telescope, the position angle of the beam is tilted when the focal chariot is moving away from the meridian. For the NRT, the correct expression for the PA is $PA = \arcsin(\sin(AH) \times \sin\delta)$, where AH is the hour angle. The AH from the meridian transit being less than 30 min, the tilt never exceeds 7.5° (or even 4.8° in our case given the actual distribution of our sources in declination). This results in a negligible effect on the average beam shape during a single meridian transit.

The HI flux calibration is homogeneous among the KLUN series. These measurements, however, need to be homogenized with the data from other telescope catalogs before a proper comparison can be carried out. For the HI mass function calculations, we used a shift of respectively $\Delta m_{\rm HI} = 0.27$ and $\Delta m_{\rm HI} = 0.20$ in magnitude scale between the KLUN sample $F_{\rm HI}$ measurement and those from Arecibo and Parkes samples:

$$m_{\rm HI} = -2.5\log(0.2366 {\rm F_{HI}}) + 15.84$$

$$m_{\rm HI-KLUN} = m_{\rm HI-Arecibo/Parkes} - \Delta m_{\rm HI}$$

Figure 3 shows the agreement between each telescope's HI magnitude scale after applying this shift.

3. HI mass function from the KLUN compilation

3.1. The $\Sigma\,(1/V_{max})$ method

The HI mass function is generally parametrized as a Schechter function of the form

$$\phi(M_{\rm HI}) = \frac{d{\rm n}}{d\log {\rm M_{HI}}} = \ln 10 \;\phi_\star \left(\frac{M_{\rm HI}}{M_\odot}\right)^{\alpha+1} {\rm e}^{-\frac{M_{\rm HI}}{M_\star}}, \qquad (1)$$

where α represents the faint-end slope, $M_\star$ is the characteristic mass, and $\phi_\star$ is the scaling or normalization density factor.

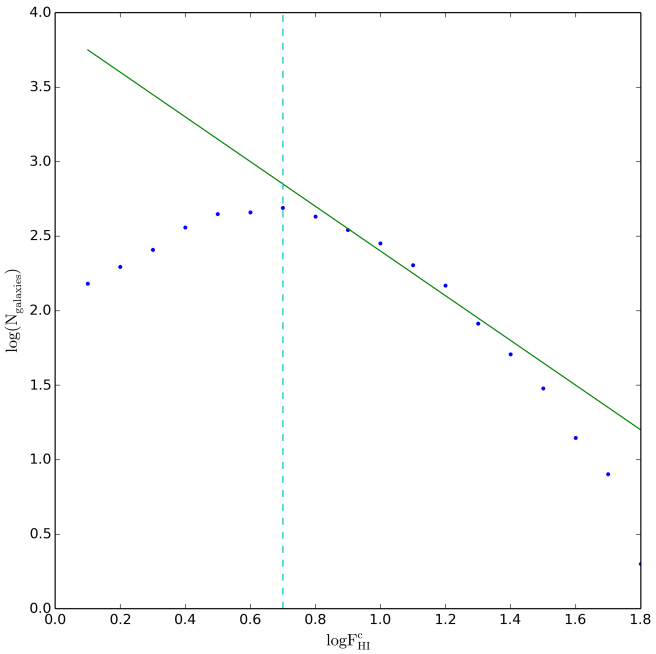

Fig. 4. Logarithmic HI flux distribution. Blue dots are the galaxy counts per 0.1 dex flux bin; the green line shows the expected growth for a pure flux limited sample. The vertical blue dashed line marks the flux limit adopted.

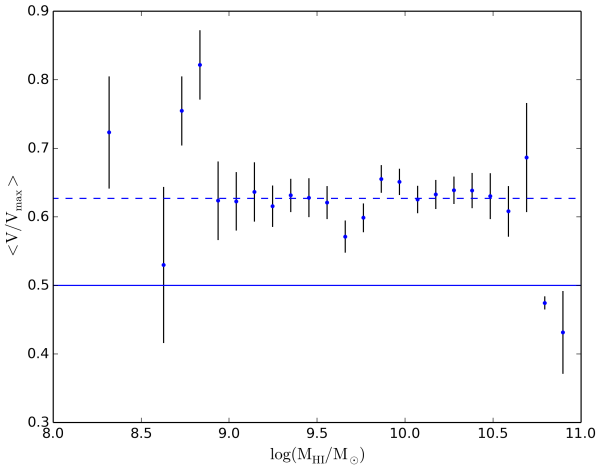

Fig. 5. Mean value $< V/V_{max} >$ binned by HI mass. Error bars are Poisson counting uncertainties. The solid line indicates the value of 0.5 expected for a homogeneous spatial distribution. The dashed line shows the actual average value from the KLUN catalog limited to $\log({\rm F_{HI}}) \geq 0.7$.

To calculate this function we have chosen the simplest way, the so-called $\Sigma\,(1/V_{max})$ method (Schmidt (1968)), which for a flux limited sample, provides an equivalent of a volume limited catalog. In this method, the source count is weighted by the maximum volume V_{max} in which a galaxy of a given HI mass can be detected by the instrument and included in the sample. The value of $\phi(M_{\rm HI})$ in a given $M_{\rm HI}$ bin is then obtained by the sum of $1/V_{max,i}$ for all galaxies in that bin.

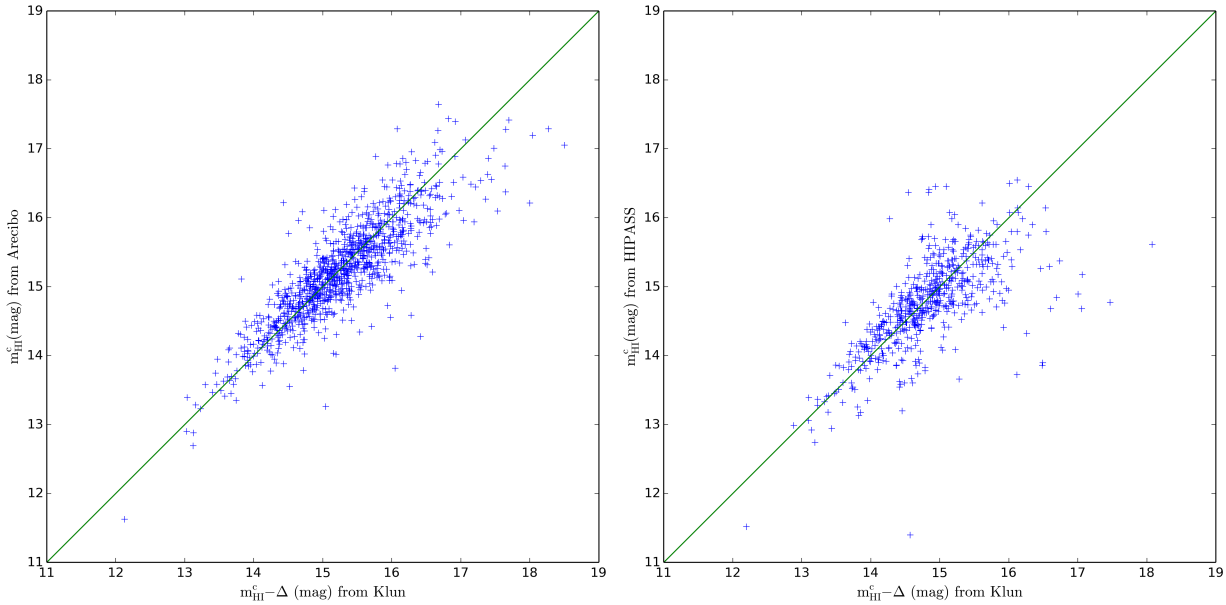

Fig. 3. Comparison of some of our HI-flux values with some independent measurements from Springob et al. (2005) and HIPASS (Meyer et al. 2004). Fluxes are expressed in magnitude $m_{\rm HI}$ scale, with $m_{\rm HI} = -2.5\log(0.2366{\rm F_{HI}}) + 15.84$, as in Paturel et al. (2003b). The green line shows the first diagonal.

The value of V_{max} is calculated as

$$V_{max}(M_{HI}) = \frac{4\pi f_{sky}}{3}\left[\frac{M_{\rm HI}}{M_\odot}\frac{1}{2.36\times10^5 F_{\rm HIlim}}\right]^{3/2} \quad {\rm Mpc}^3, \quad (2)$$

where $F_{\rm HIlim}$ is the flux limit of the HI survey (assumed complete in flux) and f_{sky} is the sky fraction surveyed. Here, by construction, an imprecision in these two terms directly translates into an imprecision in the normalization density $\phi_\star$.

In principle, for a blind survey, f_{sky} should be calculated as the sum of all Nançay beam areas on the sky. The Nançay beam size varies with declination so that the half power beam size is 4' × 22' for $\delta \leq 25°$ and 4' × 18'/sin(69.132-δ/2) for δ ¿ 25°. This would give us an $f_{sky,t} = 2.74\ 10^{-3}$ for the whole composite Nançay sample (where "t" stands for "targeted"). We know that this number is not the actual f_{sky}, since the sample is optically/NIR selected and KLUN galaxy targets have been chosen so that no HI measurement was known in the literature at the time of the observation sample definition. However, we can deduce the actual f_{sky} from the normalization factor necessary to compare the HI mass function obtained from a targeted survey with the value obtained from a pure blind search catalog. This is done by forcing the KLUN HI mass Schechter function to have the same $\log(\phi_*)$ as that from the ALFALFA catalog, which is used here as the reference blind survey. From this $\log(\phi_*)$ comparison, we get a factor of 112 on f_{sky}, which thus becomes $f_{sky} = f_{sky,t} \times 112 = 0.307$ for the actual value to be used in Eq. (2).

Using the $\Sigma(1/V_{max})$ method requires two main assumptions: 1) we control the selection of the catalog, and 2) the space distribution of the sources is not too far from homogeneity. To deal with the first point, we forced a sharp cutoff to the KLUN Nançay HI-catalog at the apparent completeness limit $\log({\rm F_{HI}}) \geq 0.7$ (see Fig. 4). We assume here that this limit in HI flux is stronger than the optical or NIR selection limit of the parent sample used to define the radio follow-up program. We note that this is not necessarily true for the very low surface brightness population. Concerning the second point, the low spatial resolution of single-dish observations at 1.4 GHz leads to HI line confusion at the scale of the antenna beam ($\equiv 4' \times 22'$) and limits high spatial clustering of HI catalogs. Fig. 1 shows the kinematical distance distribution of the sample. The distribution is rather smoothed with a few peaks emerging at 2 500 km.s^{-1}, 3 800-5 000 km.s^{-1}, 5 700 km.s^{-1}, and 6 800 km.s^{-1}, which correspond to the main supercluster concentrations known in the area visible from Nançay (e.g., respectively Hydra and Antlia clusters, Centaurus and Perseus-Pisces complexes, Abell347 cluster, and Coma cluster). A method for controlling the deviation from a pure homogeneous spatial distribution is known as the V/V_{max} statistical test (Schmidt (1968)), which compares the actual volume within the source distance to the maximum volume in which the source might be detected. In a homogeneous volume, the expectation value $< V/V_{max} >$ is 0.5. Figure 5 shows the V/V_{max} per bin of $M_{\rm HI}$. The values are consistent with $< V/V_{max} > \equiv 0.62$ indicating the presence of overdensities, as expected from the various peaks appearing in the radial velocity distribution (Fig. 1). This suggests that the sample might be biased by the few large clusters present in this redshift domain.

Finally, as discussed in Martin et al. (2010), in the local volume where peculiar velocities are comparable to the expansion, the distance uncertainty introduced by the use of a pure Hubble flow for the distance estimate may cause distortion of the faint end of the HI mass function. The infall towards the Virgo cluster being the most important feature at this scale, we then used radial velocities corrected for a Virgo infall model, V_{Vir}, for the kinematical distance estimate. According to hyperleda [5], $V_{Vir} = V_{LG} + 208\ \cos(\theta)$,

[5] http://leda.univ-lyon1.fr/leda/param/vvir.html

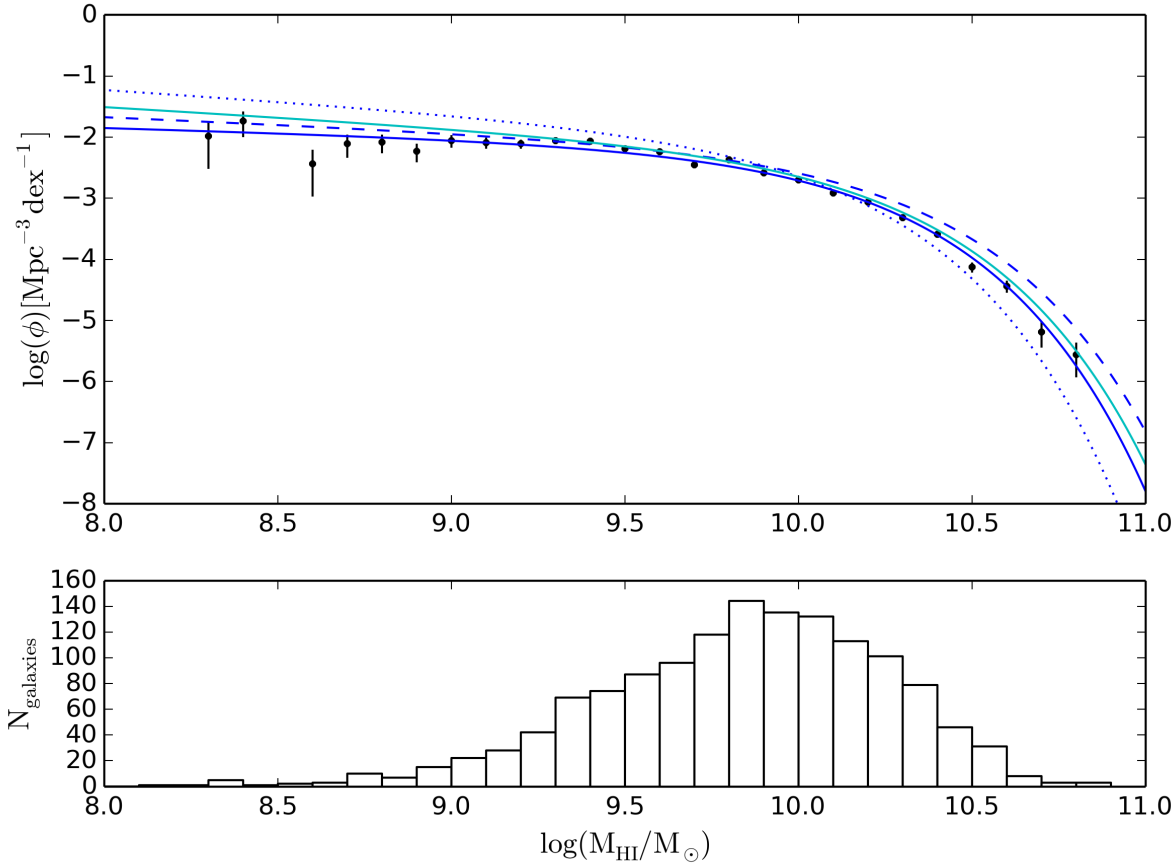

Fig. 6. HI mass function from KLUN (dark blue line) vs. Springob et al. (2005) (blue dashed line), Zwaan et al. (2005) (blue dotted line), and Haynes et al. (2011) (cyan line). KLUN and Springob results are both normalized to the ALFALFA survey. Observed values (black dots) are calculated per bins of 0.1 in $\log(M_{HI}/M_{\odot})$ with error bars from the Poisson law, and the corresponding population is shown as a histogram in the bottom panel.

where V_{LG} is the velocity relative to the Local Group, 208 km.s^{-1} is the infall velocity of the Local Group according to Theureau et al. (1998b) and Terry et al. (2002), and θ is the angular distance between the observed direction and the direction of the center of the Virgo cluster (SG 104,-2 or J123310+112152).

3.2. Results

We show in Fig. 6 the HI mass function calculated for the whole flux limited sample, and the corresponding Schechter function together with three previous results from Springob et al. (2005), Zwaan et al. (2005), and Martin et al. (2010). The HI mass scale has been homogenized between the different references to take into account the shift measured between Arecibo, Nançay, and Parkes HI fluxes discussed in paragraph 2.2.

For the KLUN sample, we obtain the following parameter values (after normalization on f_{sky} according to the previous section)

$$\alpha = -1.16, \quad \log\left(\frac{\mathrm{M}_\star}{\mathrm{M}_\odot}\right) = 9.90, \quad \phi_\star = 3.12\ 10^{-3}\ \mathrm{Mpc}^{-3},$$

In Fig. 6, the KLUN and Springob et al. (2005) HI mass functions have been normalized to the same $\phi_\star$ derived for ALFALFA Martin et al. (2010). For these two catalogs, which are based on targeted observations and not on a blind HI search, the sky filling factor is not directly available or comparable owing to the selection and identification process based on optical or NIR selection (see previous section). The result from HIPASS, which is also a blind HI survey, is shown without any normalization.

4. Conclusions

We have presented here the last HI data release of a long series of observations with the NRT in the context of Tully-Fisher applications. A large fraction of these remaining 828 galaxies of the program is a compilation of low S/N or problematic cases; however, this subset contains 417 ($\sim 50\%$) of good and high quality HI line profile measurements (classes A and B). Together with the previous publications from the same observational program (KLUN), we have produced – as a by-product of the original Tully-Fisher program – a homogeneous sample of HI-fluxes for 4876 spiral galaxies, which constitutes a useful catalog for HI mass functions studies. This catalog is complete down to an HI flux of 5 Jy km.s^{-1} and samples the radial velocity space between 2000 and 8000 km.s^{-1}.Mpc^{-1}. We finally obtain a first estimation of the Schechter parameters for the HI mass function in the range from 5 10^8 to 5 10^{10} solar masses, and we

obtain a solution which is perfectly coherent with previous studies.

Acknowledgements. The Nançay radio Observatory is operated by the Paris Observatory, associated with the French Centre National de la Recherche Scientifique (CNRS) and with the University of Orléans.

References

Bottinelli, L., Durand, N., Fouque, P., et al. 1993, A&AS, 102, 57
Bottinelli, L., Durand, N., Fouque, P., et al. 1992, A&AS, 93, 173
Bottinelli, L., Gouguenheim, L., Fouque, P., & Paturel, G. 1990, A&AS, 82, 391
di Nella, H., Paturel, G., Walsh, A. J., et al. 1996, A&AS, 118, 311
Fouque, P., Bottinelli, L., Gouguenheim, L., & Paturel, G. 1990, ApJ, 349, 1
Haynes, M. P., Giovanelli, R., Martin, A. M., et al. 2011, AJ, 142, 170
Jarrett, T.-H., Chester, T., Cutri, R., et al. 2000, AJ, 120, 298
Martin, A. M., Papastergis, E., Giovanelli, R., et al. 2010, ApJ, 723, 1359
Meyer, M. J., Zwaan, M. A., Webster, R. L., et al. 2004, MNRAS, 350, 1195
Paturel, G., Petit, C., Prugniel, P., et al. 2003a, A&A, 412, 45
Paturel, G., Theureau, G., Bottinelli, L., et al. 2003b, A&A, 412, 57
Paturel, G., Vauglin, I., Petit, C., et al. 2005, A&A, 430, 751
Schmidt, M. 1968, ApJ, 151, 393
Springob, C. M., Haynes, M. P., Giovanelli, R., & Kent, B. R. 2005, ApJS, 160, 149
Terry, J. N., Paturel, G., & Ekholm, T. 2002, A&A, 393, 57
Theureau, G., Bottinelli, L., Coudreau-Durand, N., et al. 1998a, A&AS, 130, 333
Theureau, G., Coudreau, N., Hallet, N., et al. 2005, A&A, 430, 373
Theureau, G., Hanski, M. O., Coudreau, N., Hallet, N., & Martin, J.-M. 2007, A&A, 465, 71
Theureau, G., Rauzy, S., Bottinelli, L., & Gouguenheim, L. 1998b, A&A, 340, 21
Zwaan, M. A., Meyer, M. J., Staveley-Smith, L., & Webster, R. L. 2005, MNRAS, 359, L30

Appendix A: HI profiles. Continuation of Figure 2

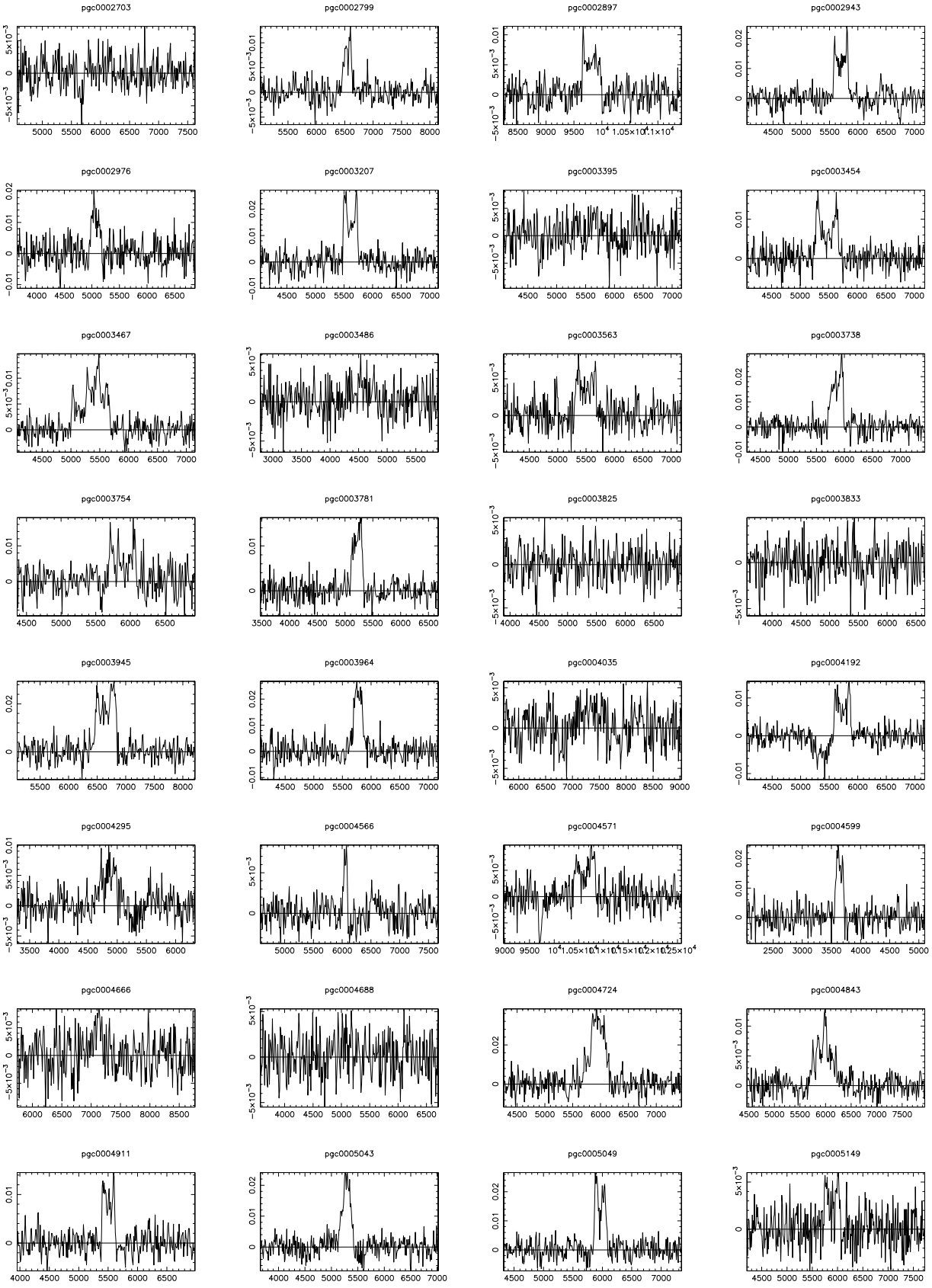

Fig. A.1. Fig. 2 **b.** HI profiles. Continuation of Fig2.

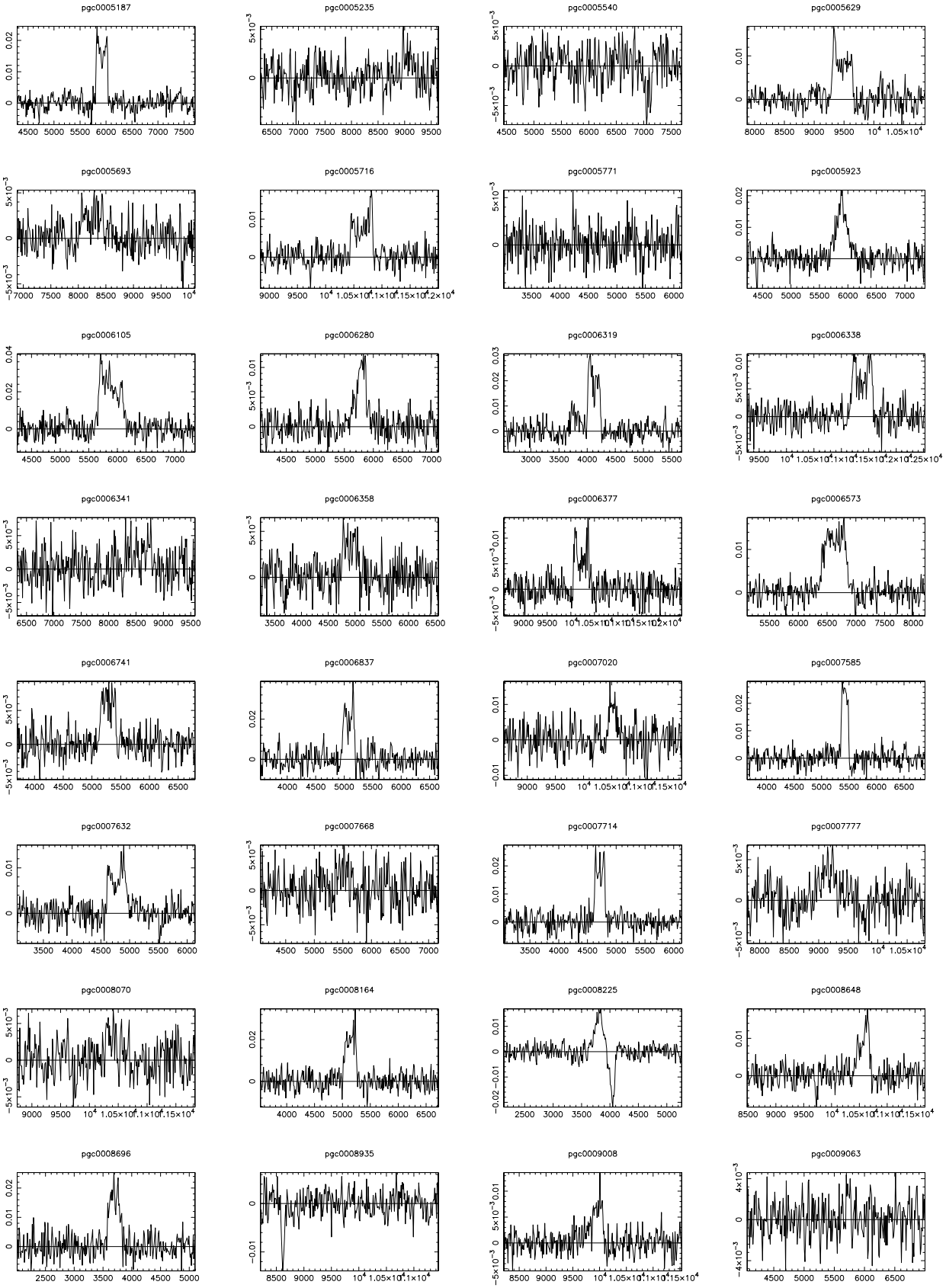

Fig. A.1. Fig. 2 **c.** HI profiles. Continued.

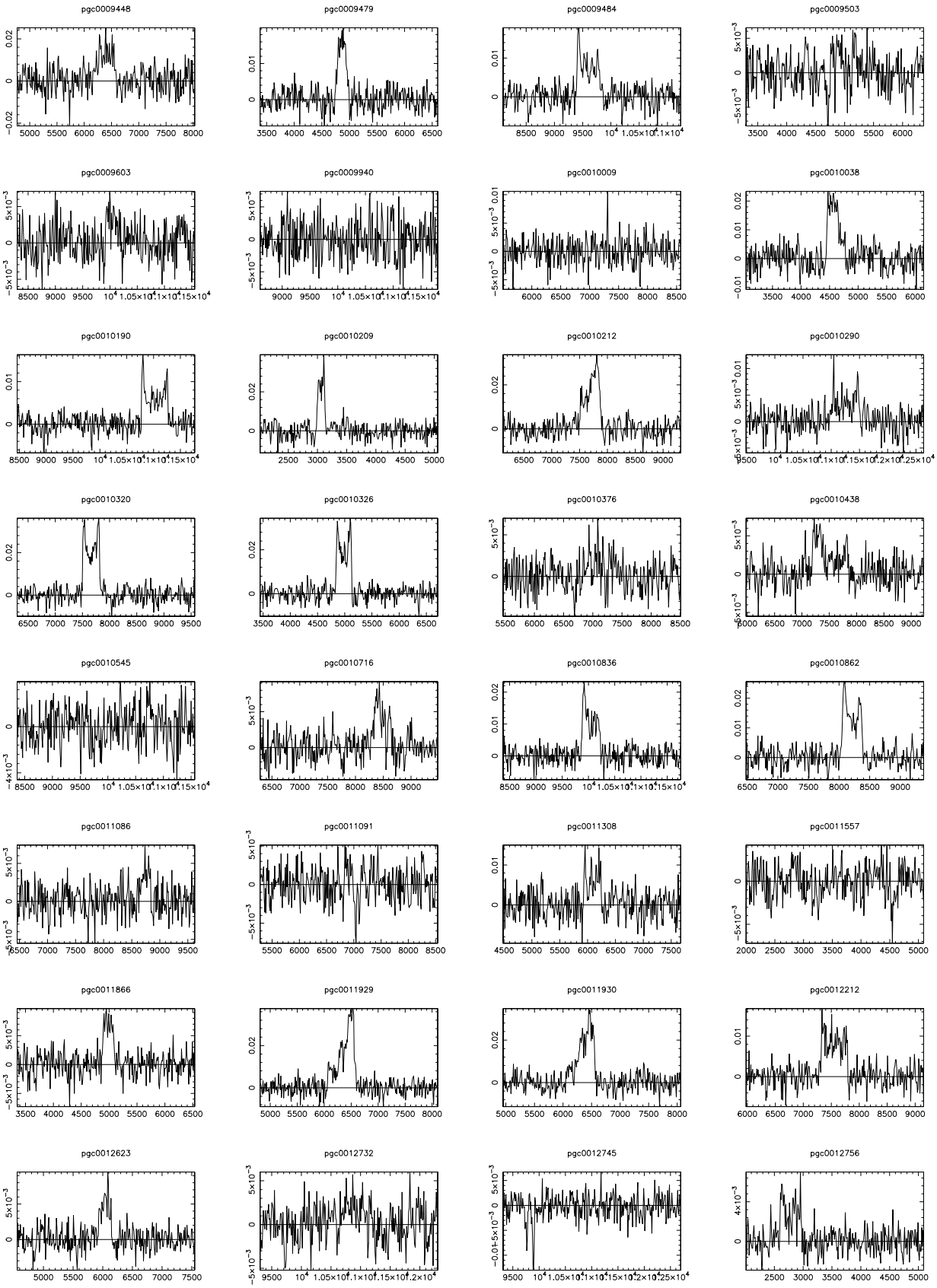

Fig. A.1. Fig. 2 **d.** HI profiles. Continued.

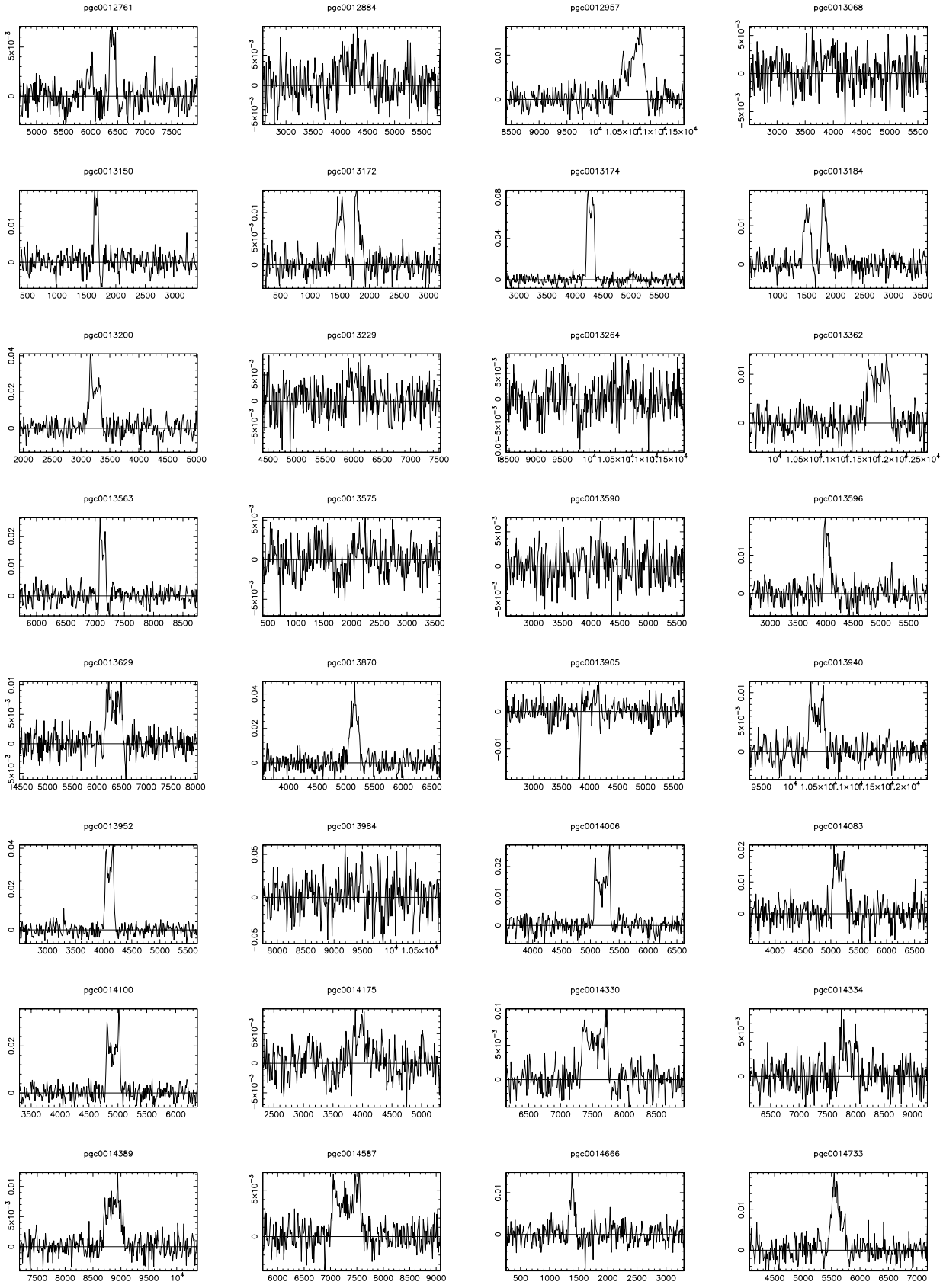

Fig. A.1. Fig. 2 **e.** HI profiles. Continued.

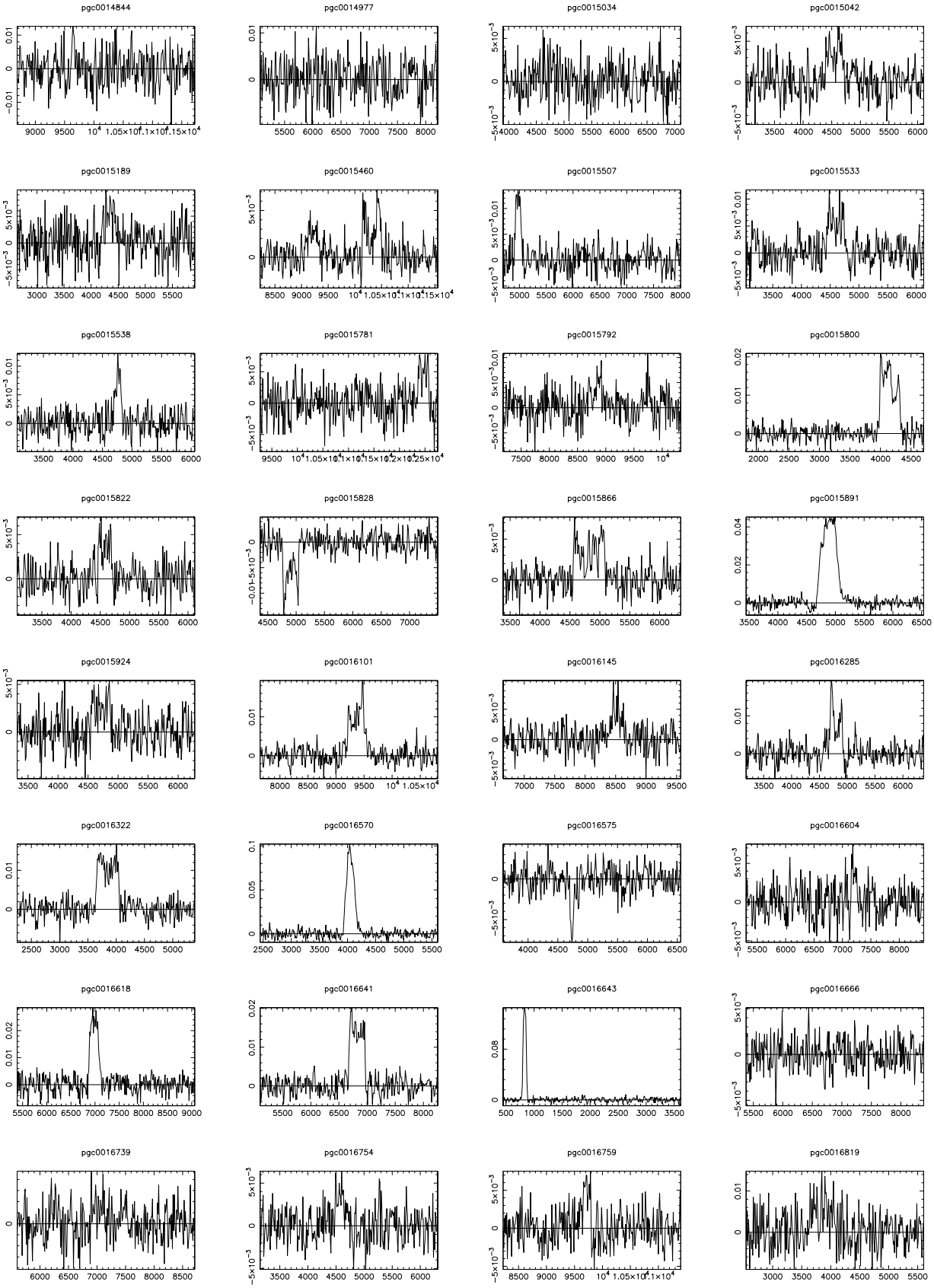

Fig. A.1. Fig. 2 **f.** HI profiles. Continued.

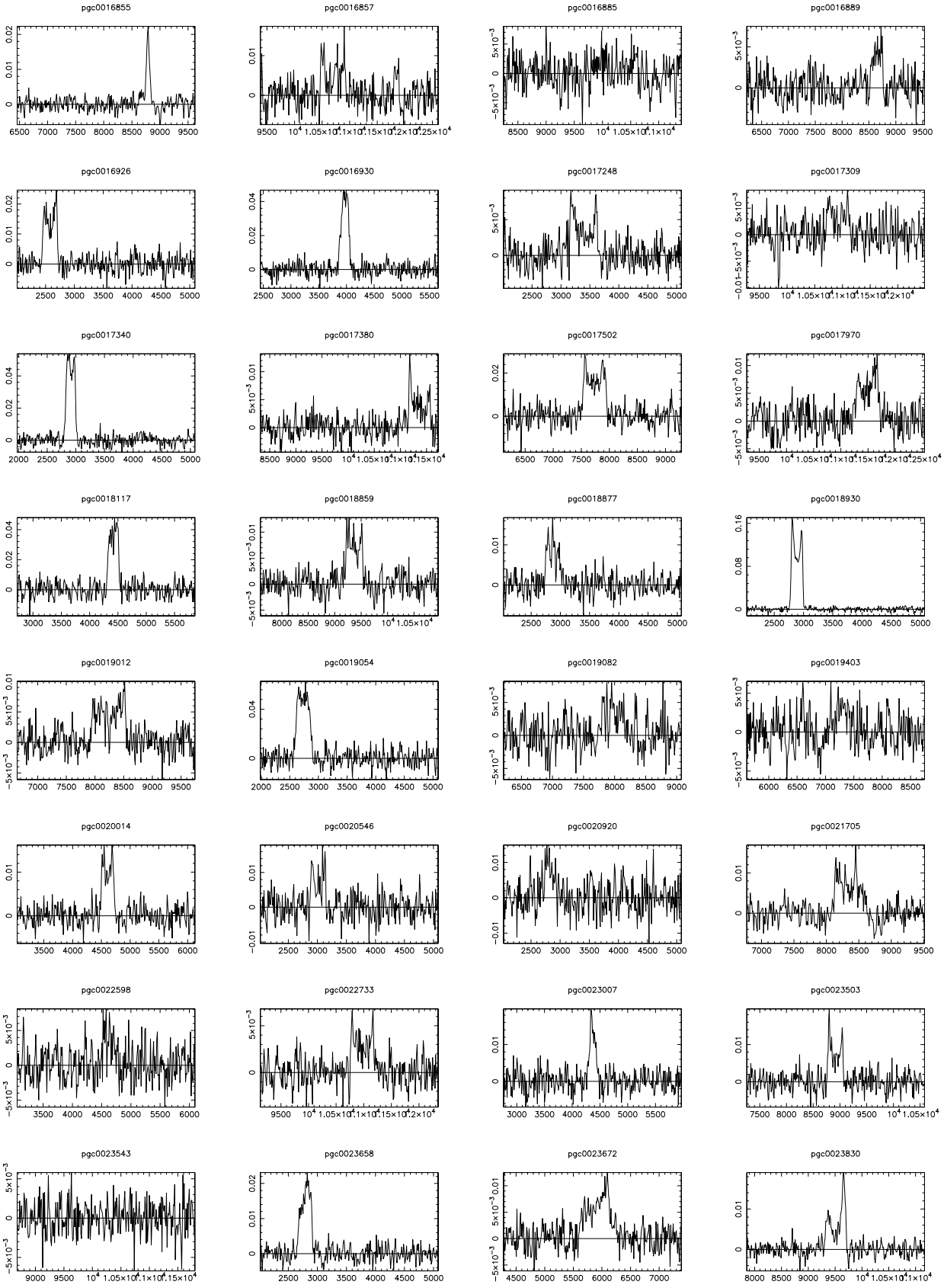

Fig. A.1. Fig. 2 **g.** HI profiles. Continued.

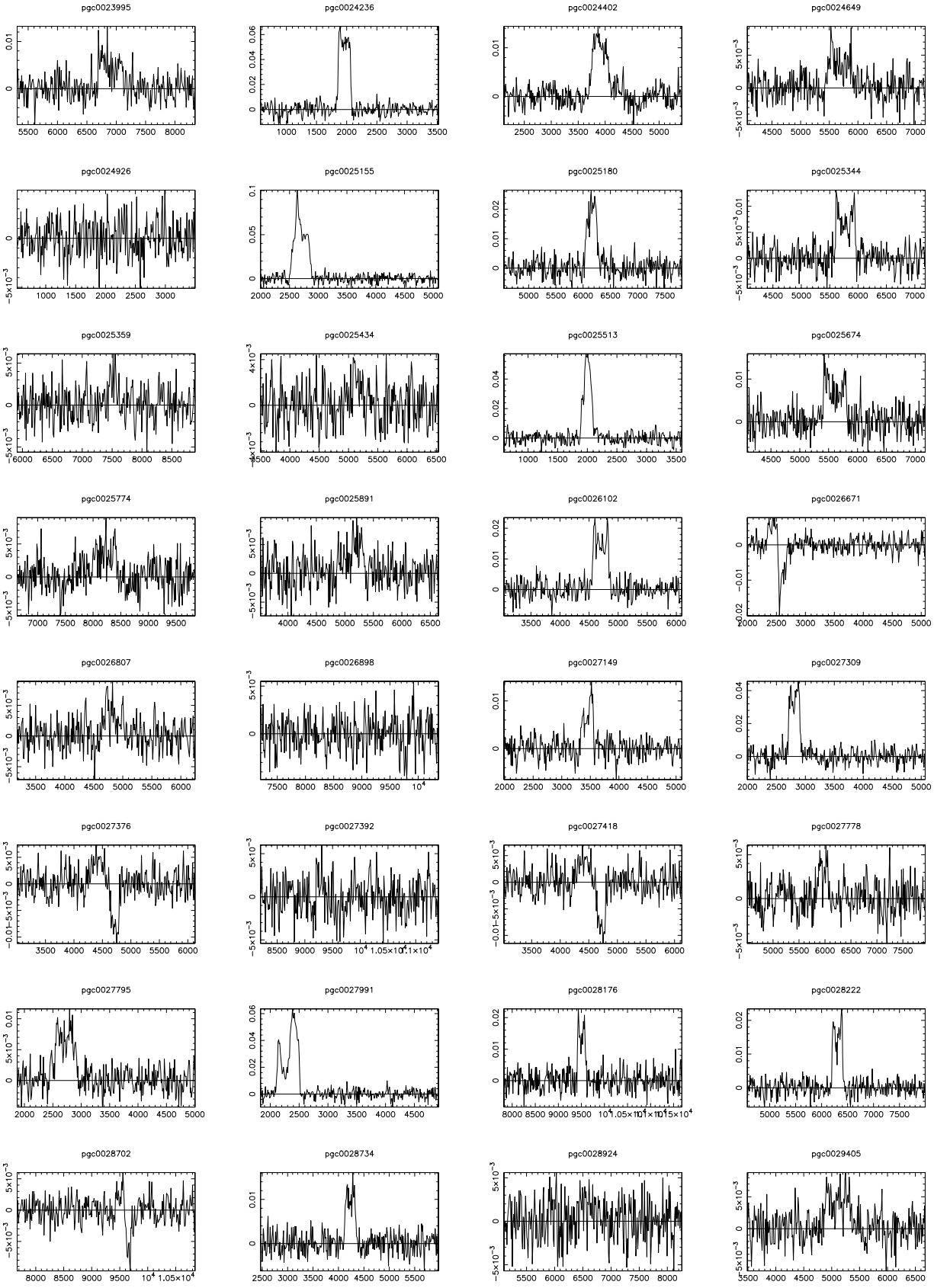

Fig. A.1. Fig. 2 **h.** HI profiles. Continued.

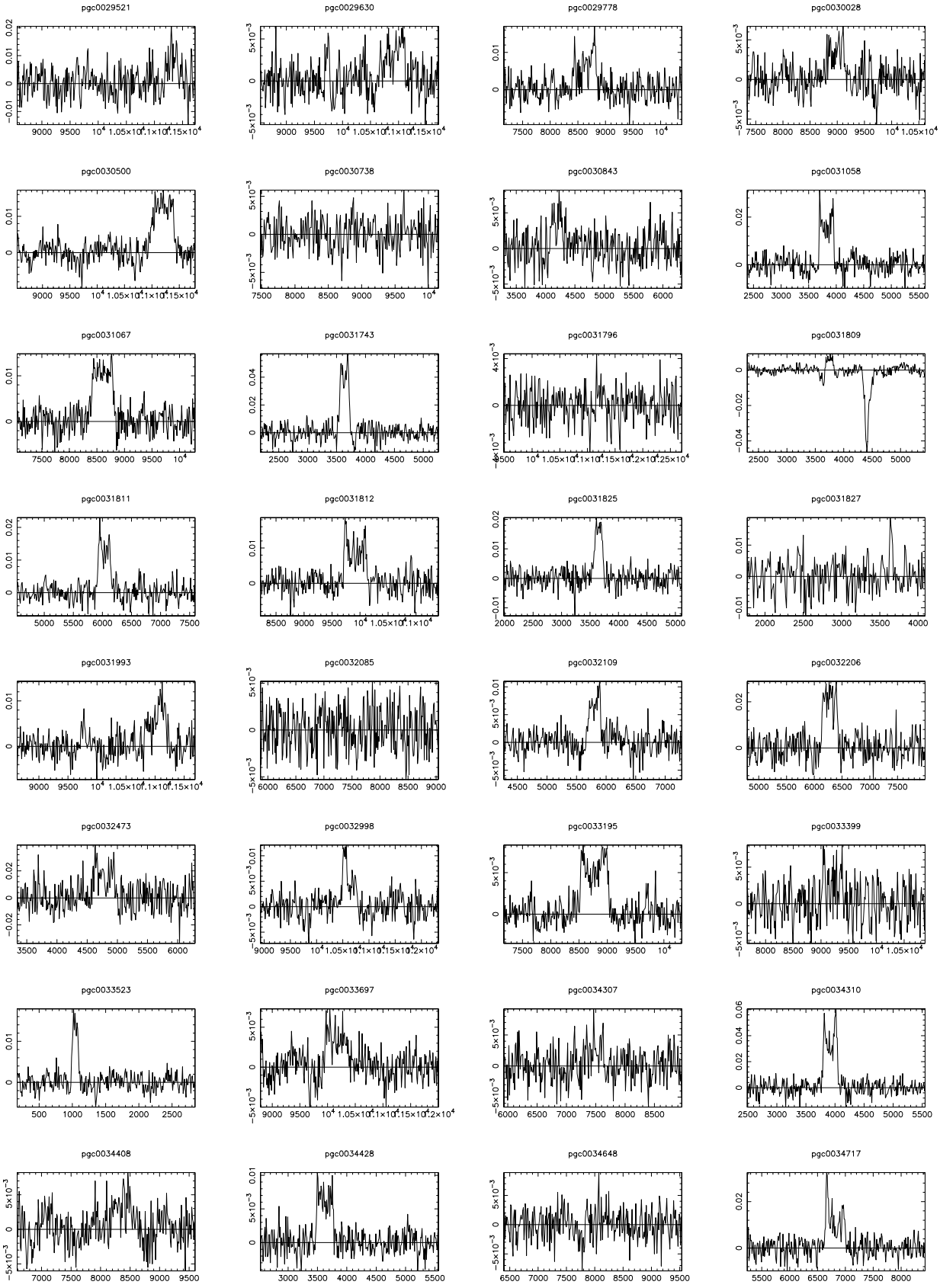

Fig. A.1. Fig. 2 **i.** HI profiles. Continued.

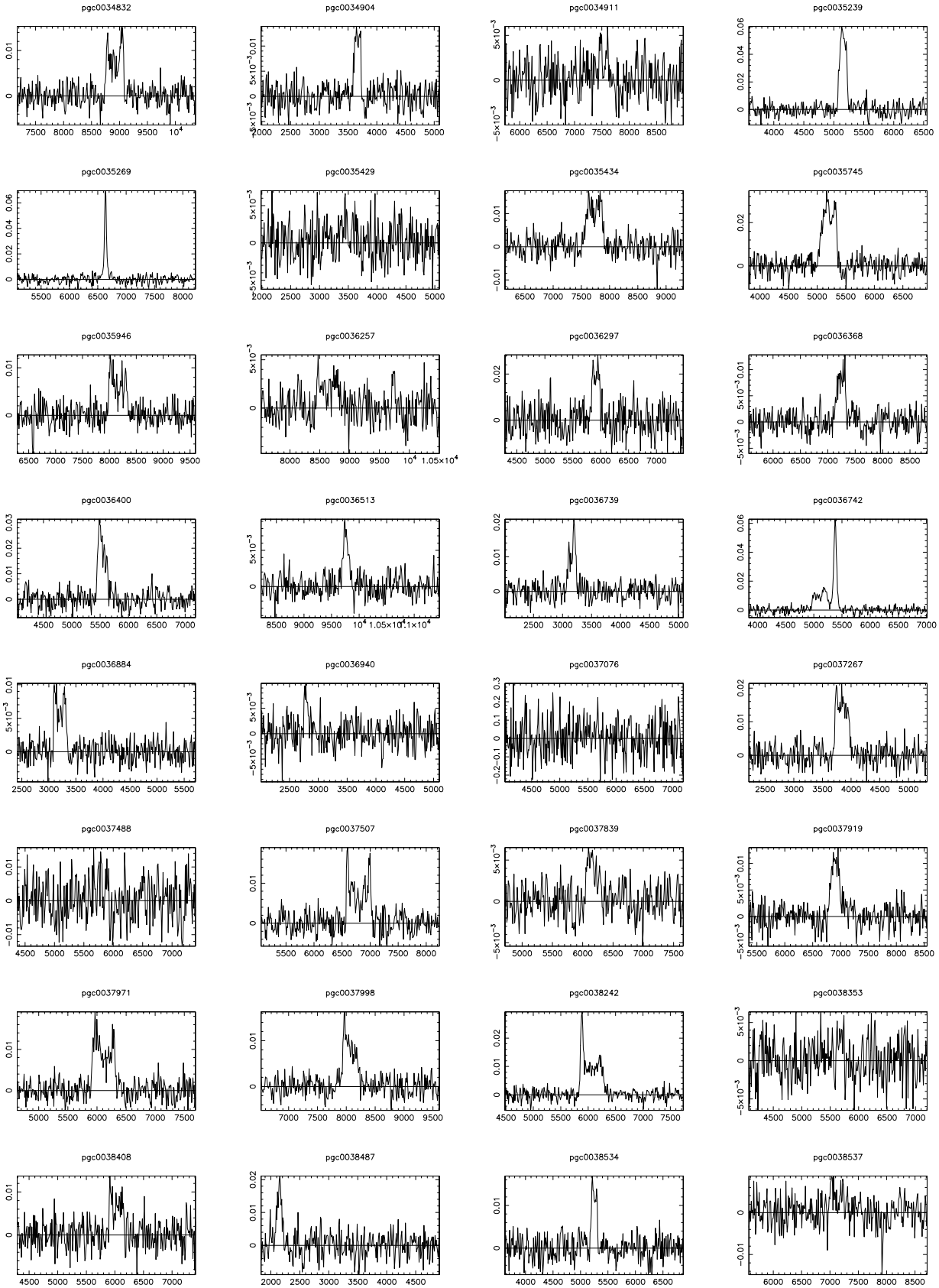

Fig. A.1. Fig. 2 **j.** HI profiles. Continued.

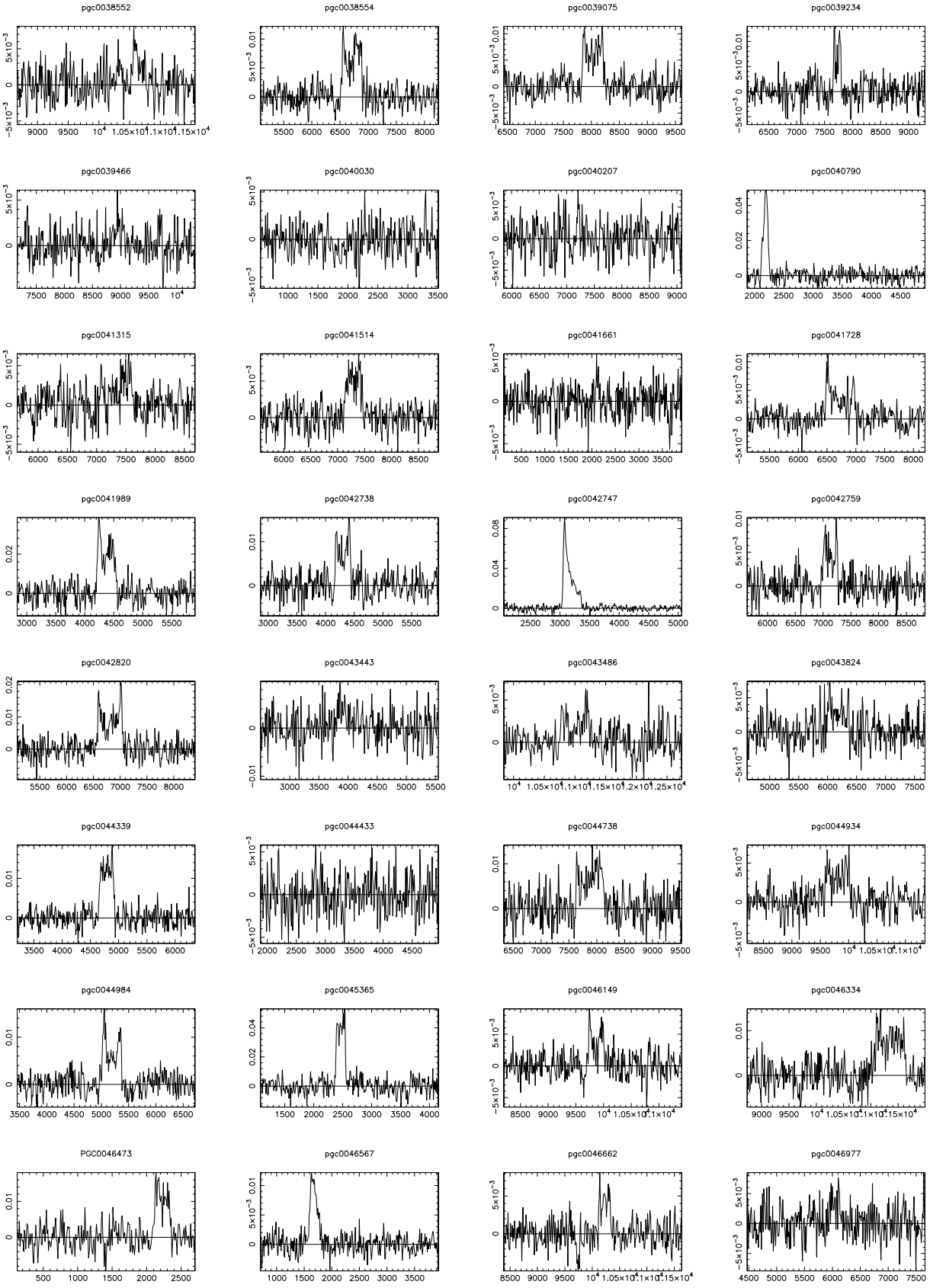

Fig. A.1. Fig. 2 **k.** HI profiles. Continued.

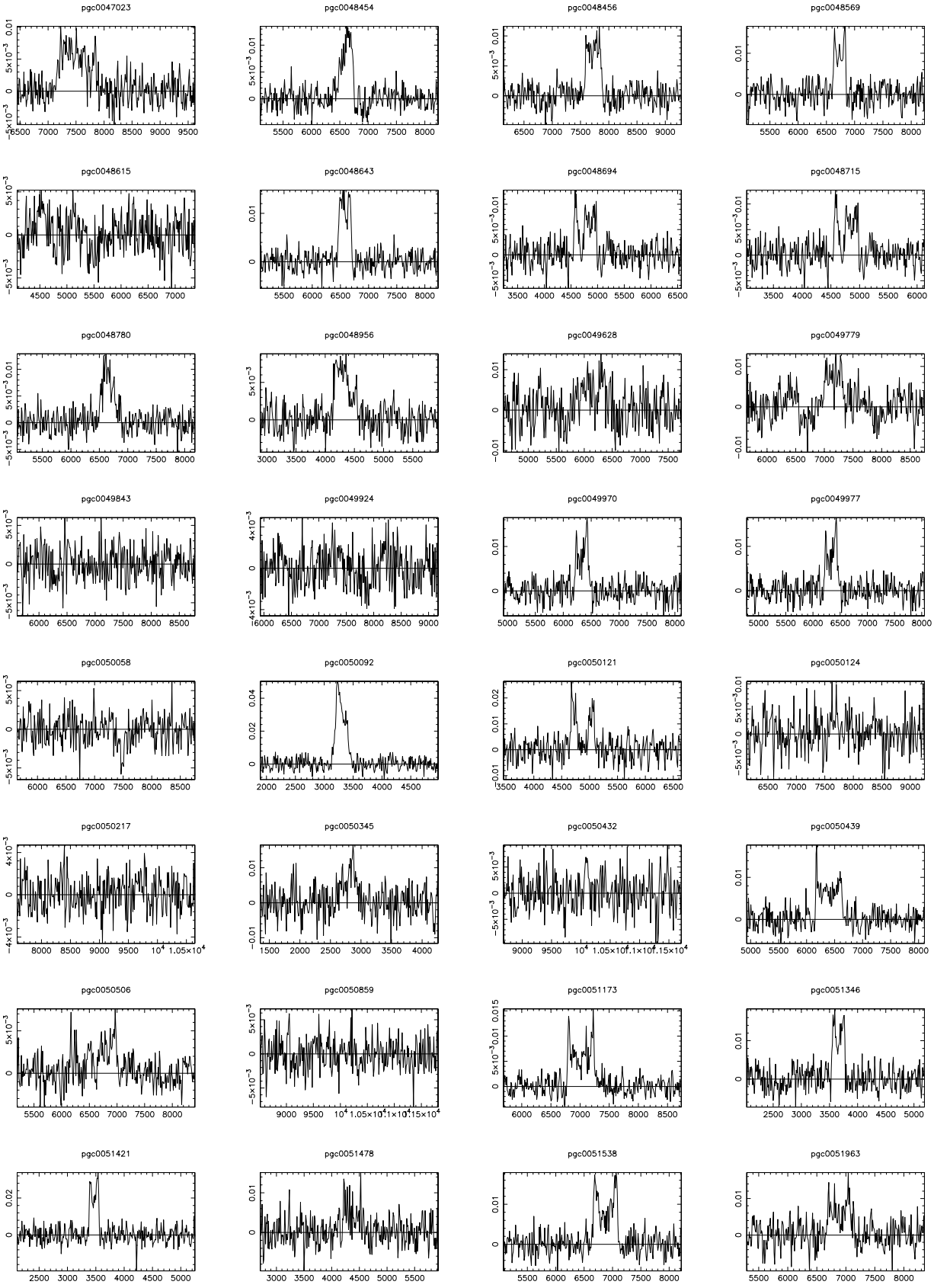

Fig. A.1. Fig. 2 l. HI profiles. Continued.

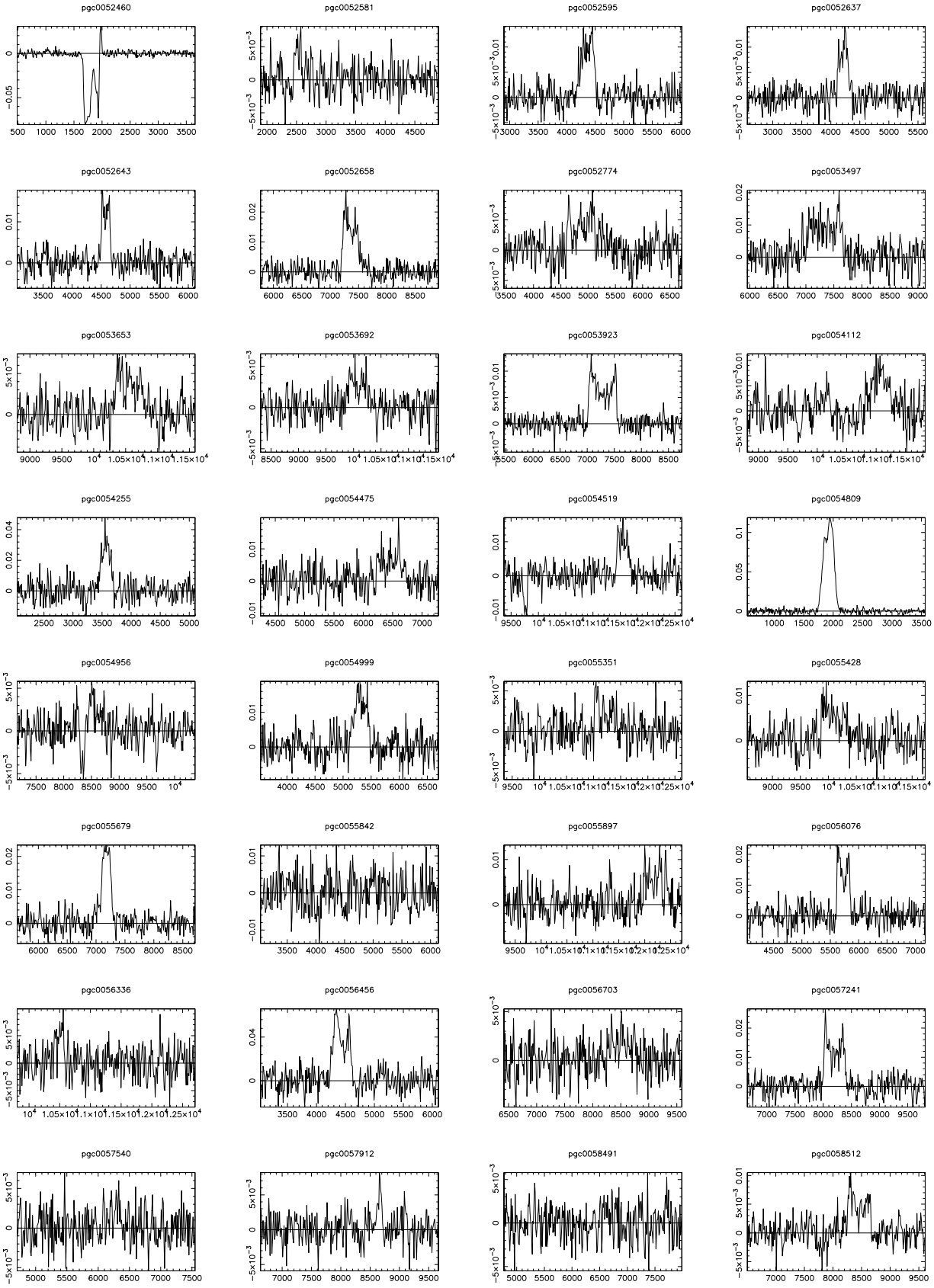

Fig. A.1. Fig. 2 **m.** HI profiles. Continued.

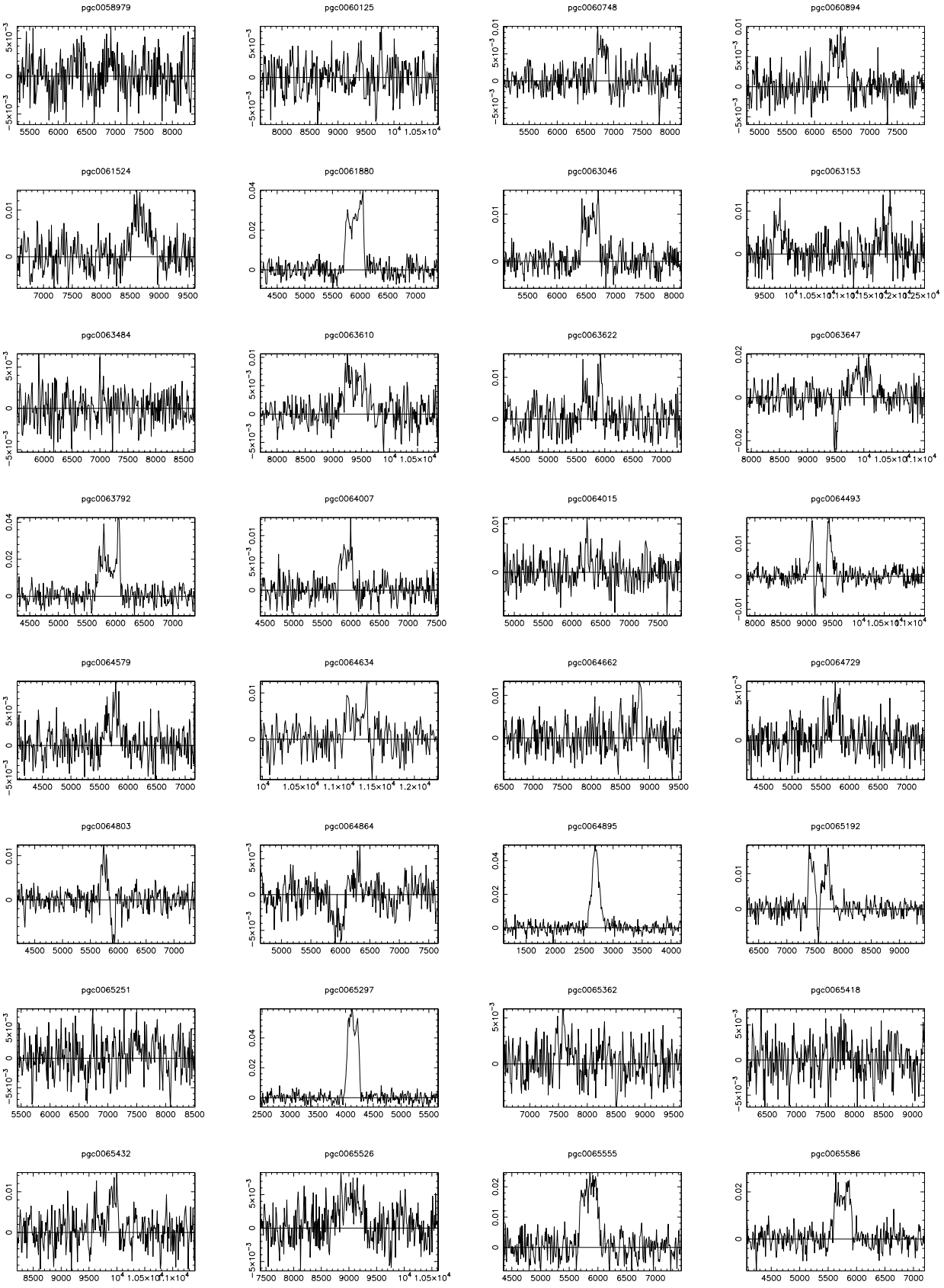

Fig. A.1. Fig. 2 **n.** HI profiles. Continued.

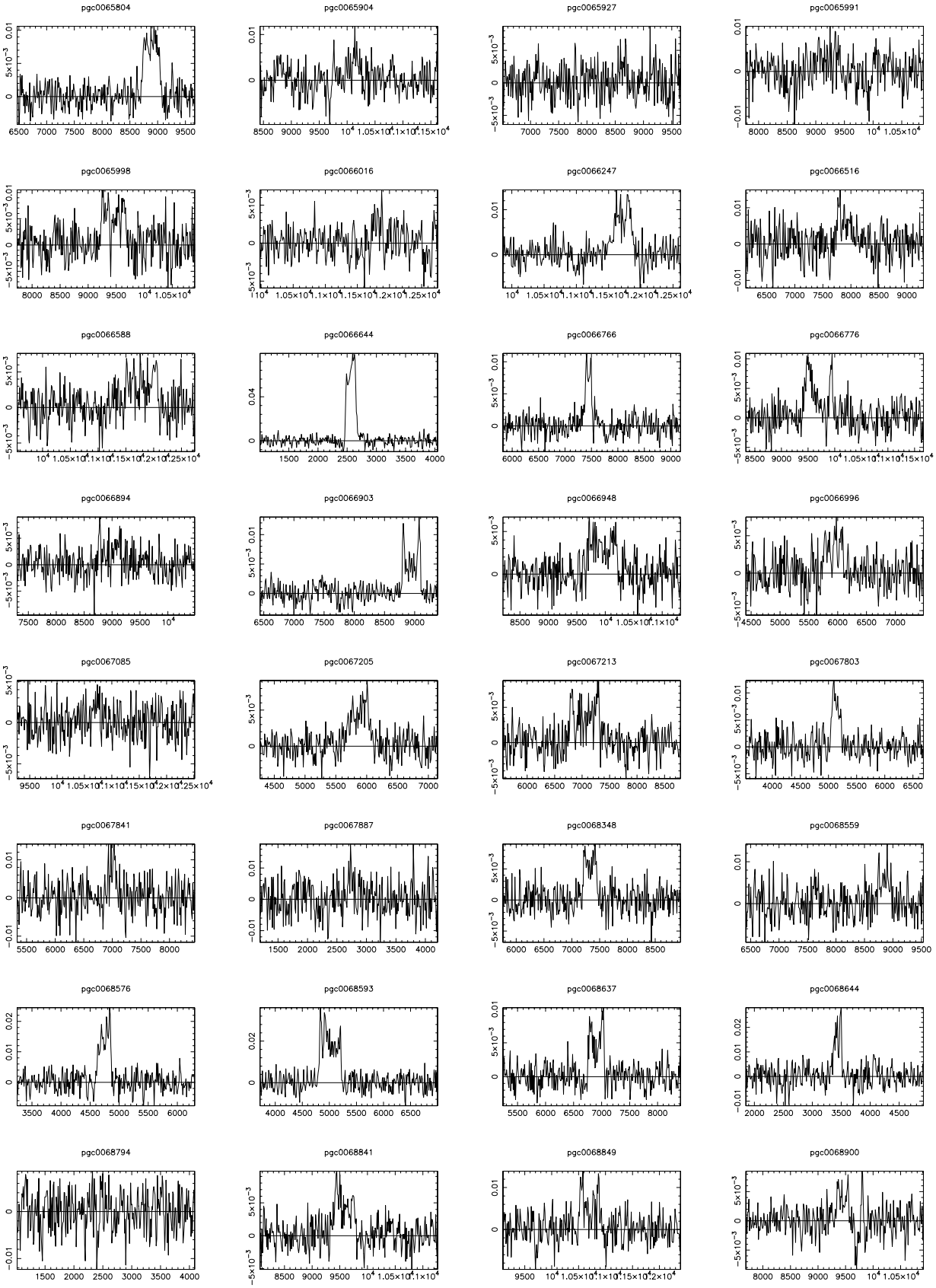

Fig. A.1. Fig. 2 **o.** HI profiles. Continued.

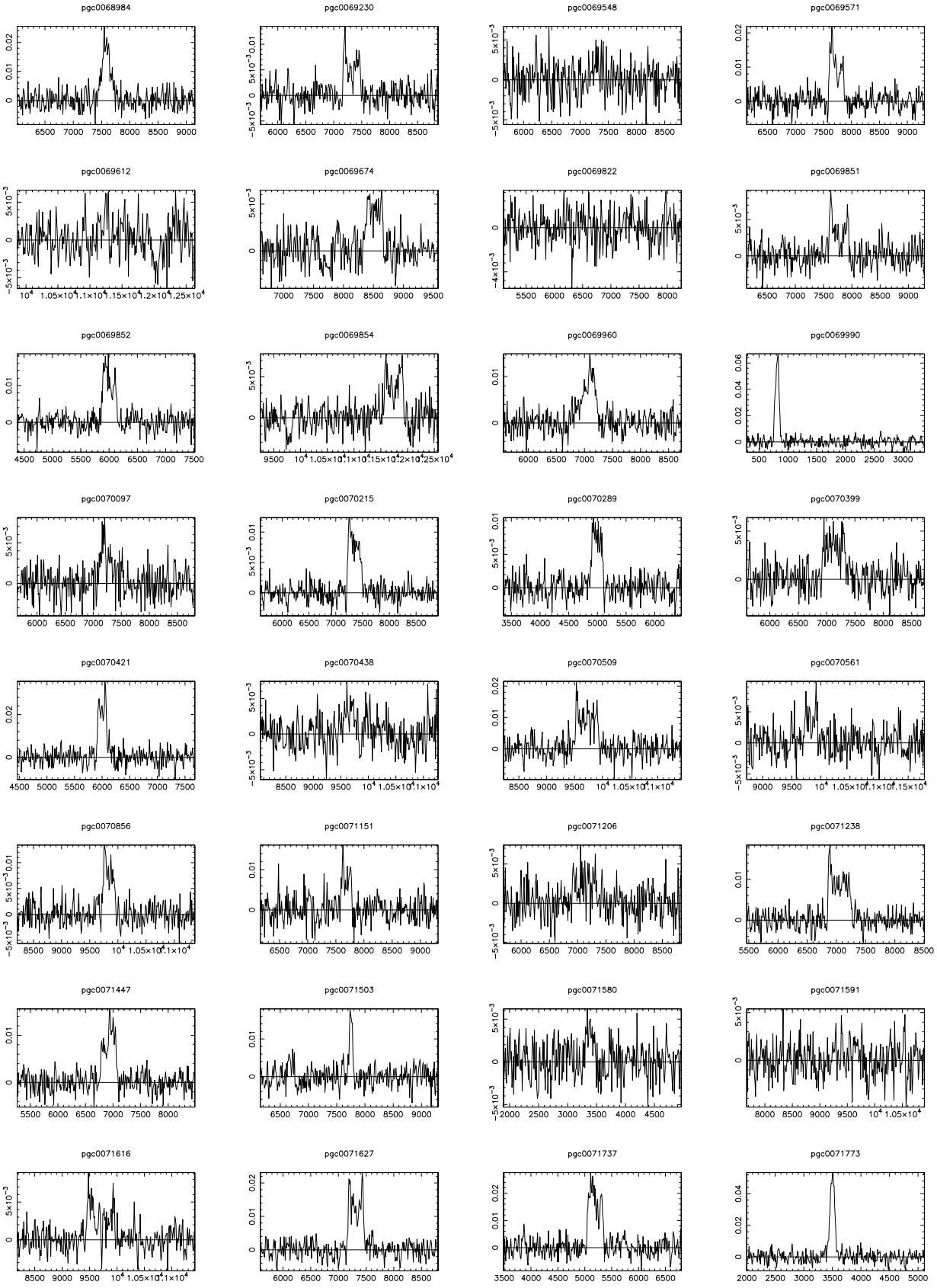

Fig. A.1. Fig. 2 **p.** HI profiles. Continued.

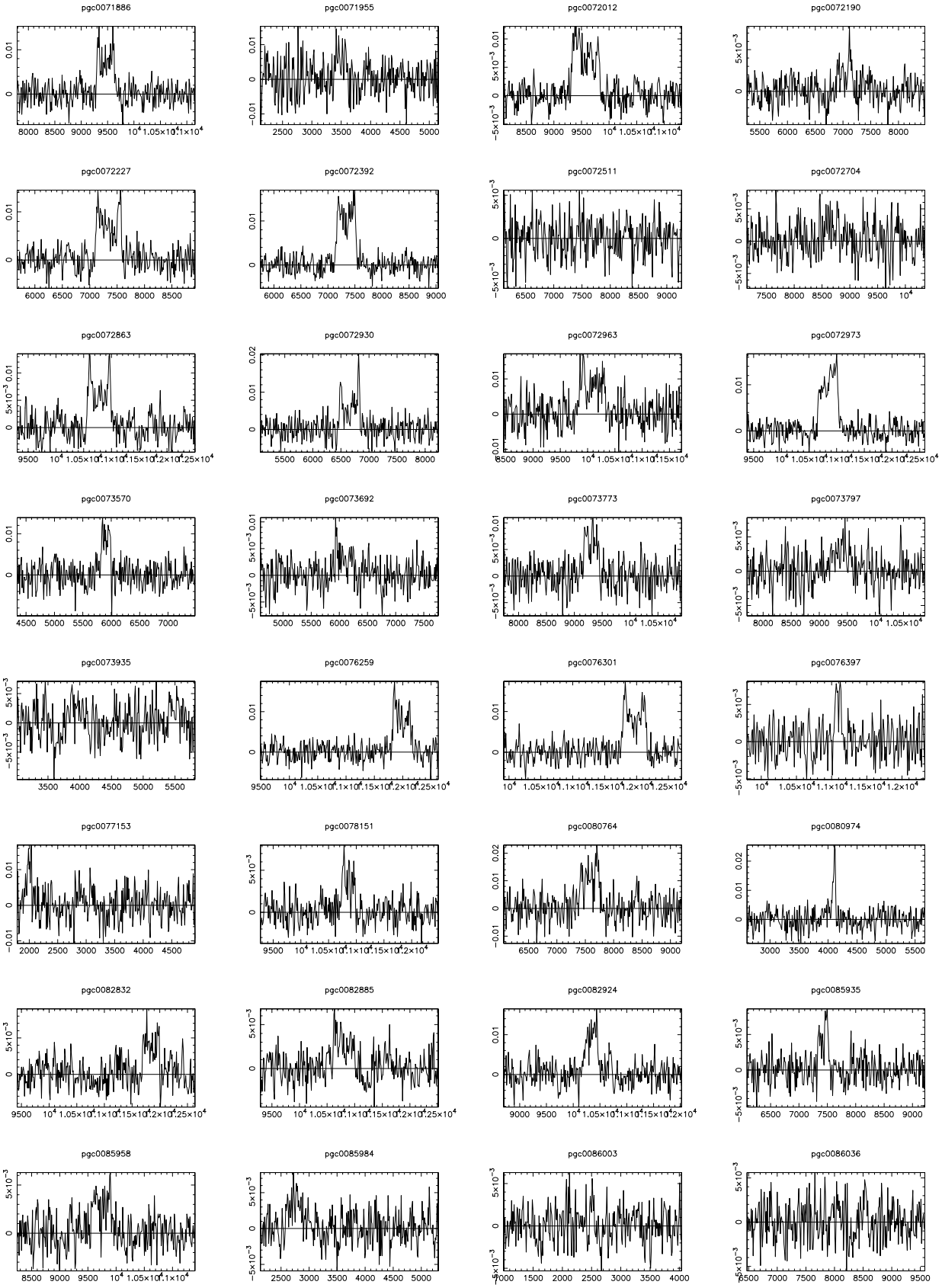

Fig. A.1. Fig. 2 **q.** HI profiles. Continued.

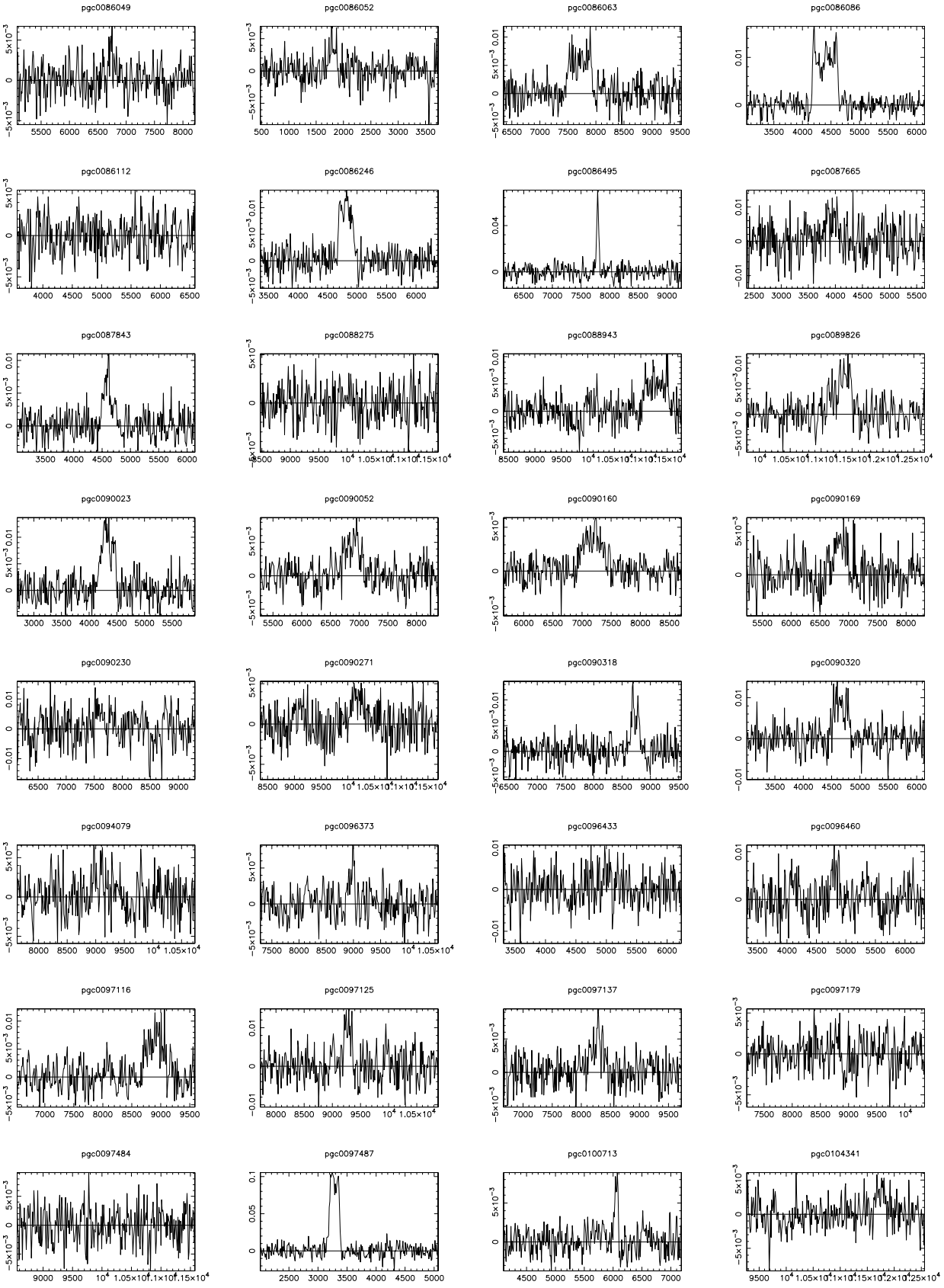

Fig. A.1. Fig. 2 **r.** HI profiles. Continued.

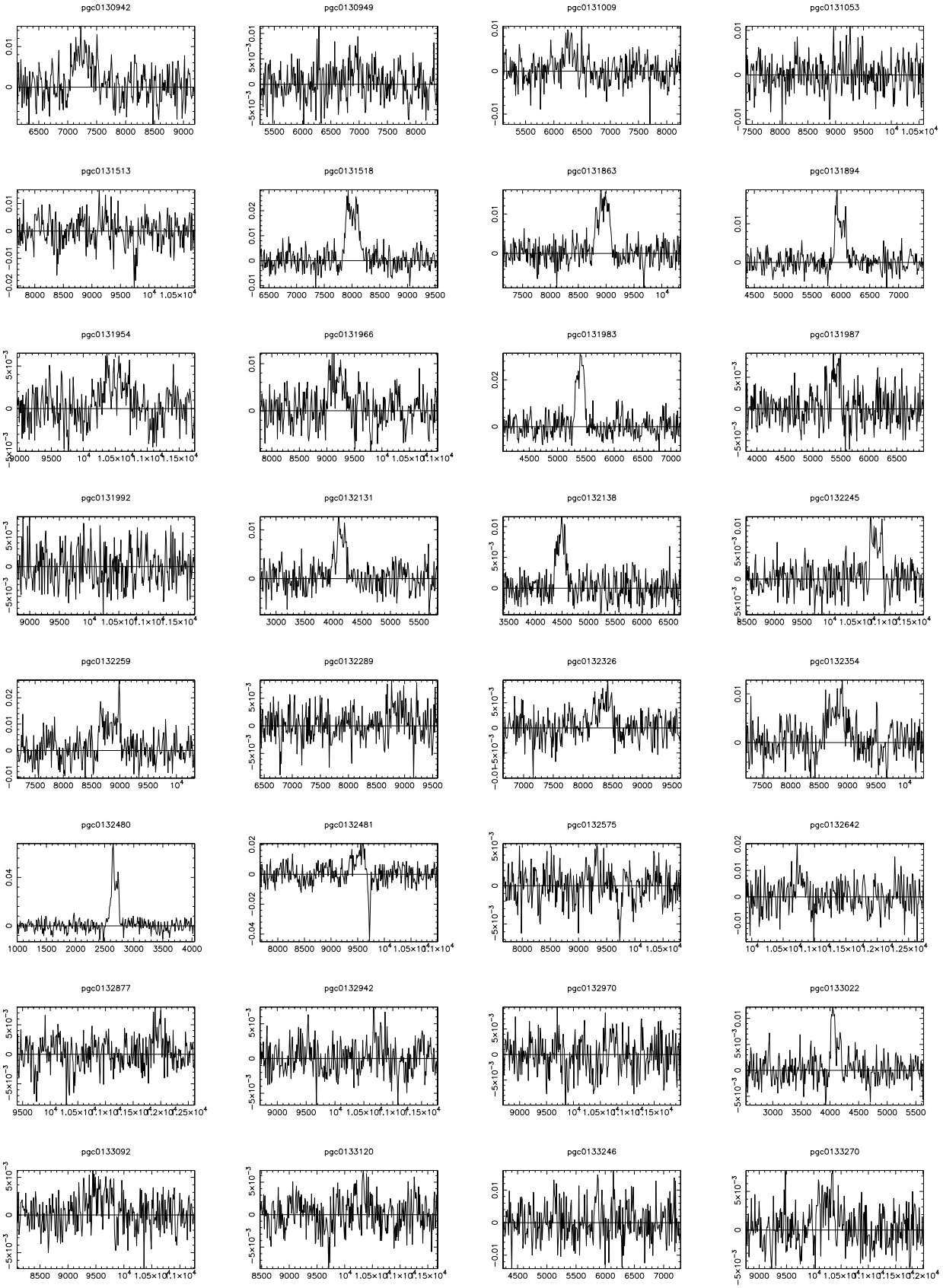

Fig. A.1. Fig. 2 **s.** HI profiles. Continued.

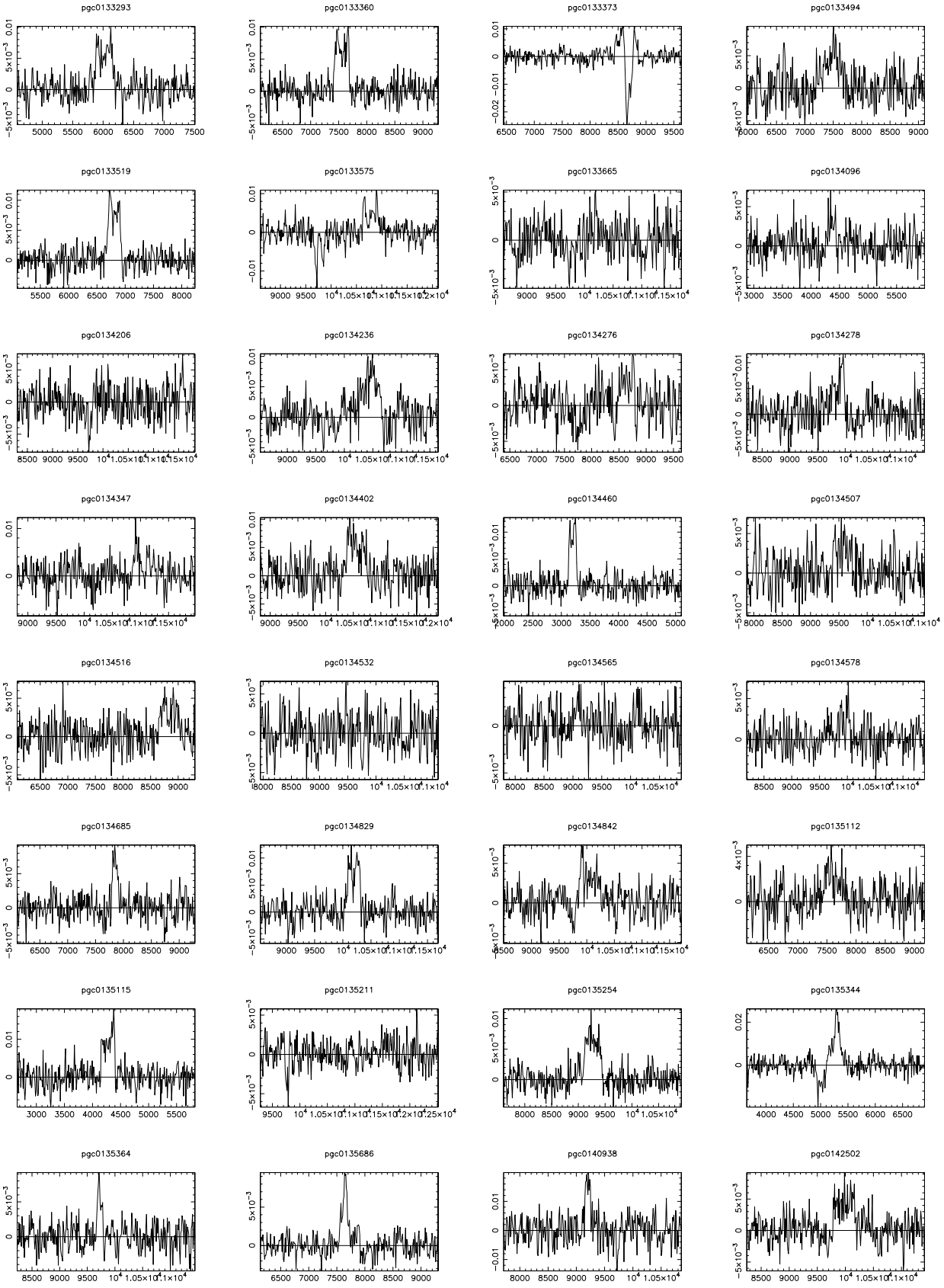

Fig. A.1. Fig. 2 **t.** HI profiles. Continued.

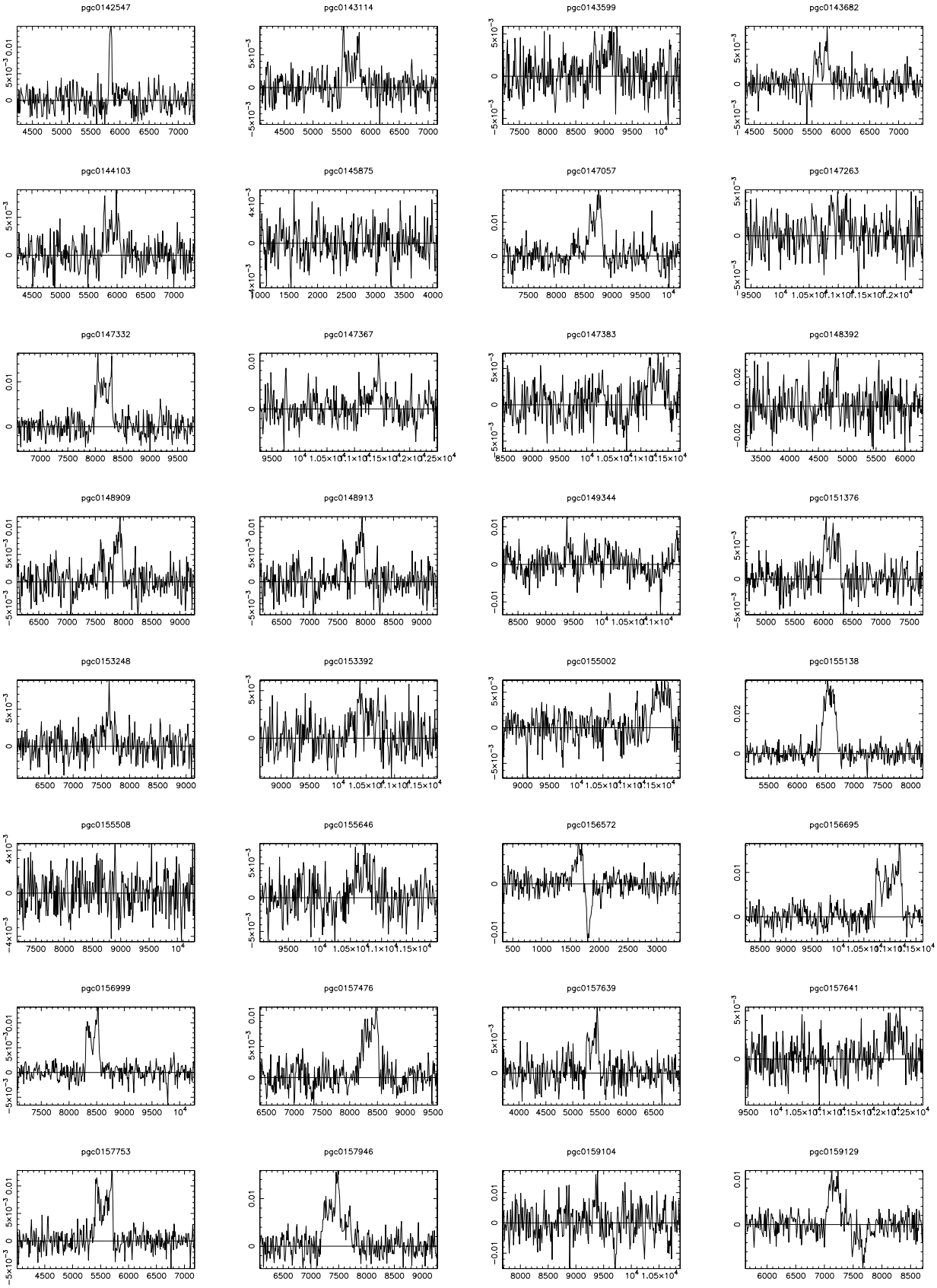

Fig. A.1. Fig. 2 **u.** HI profiles. Continued.

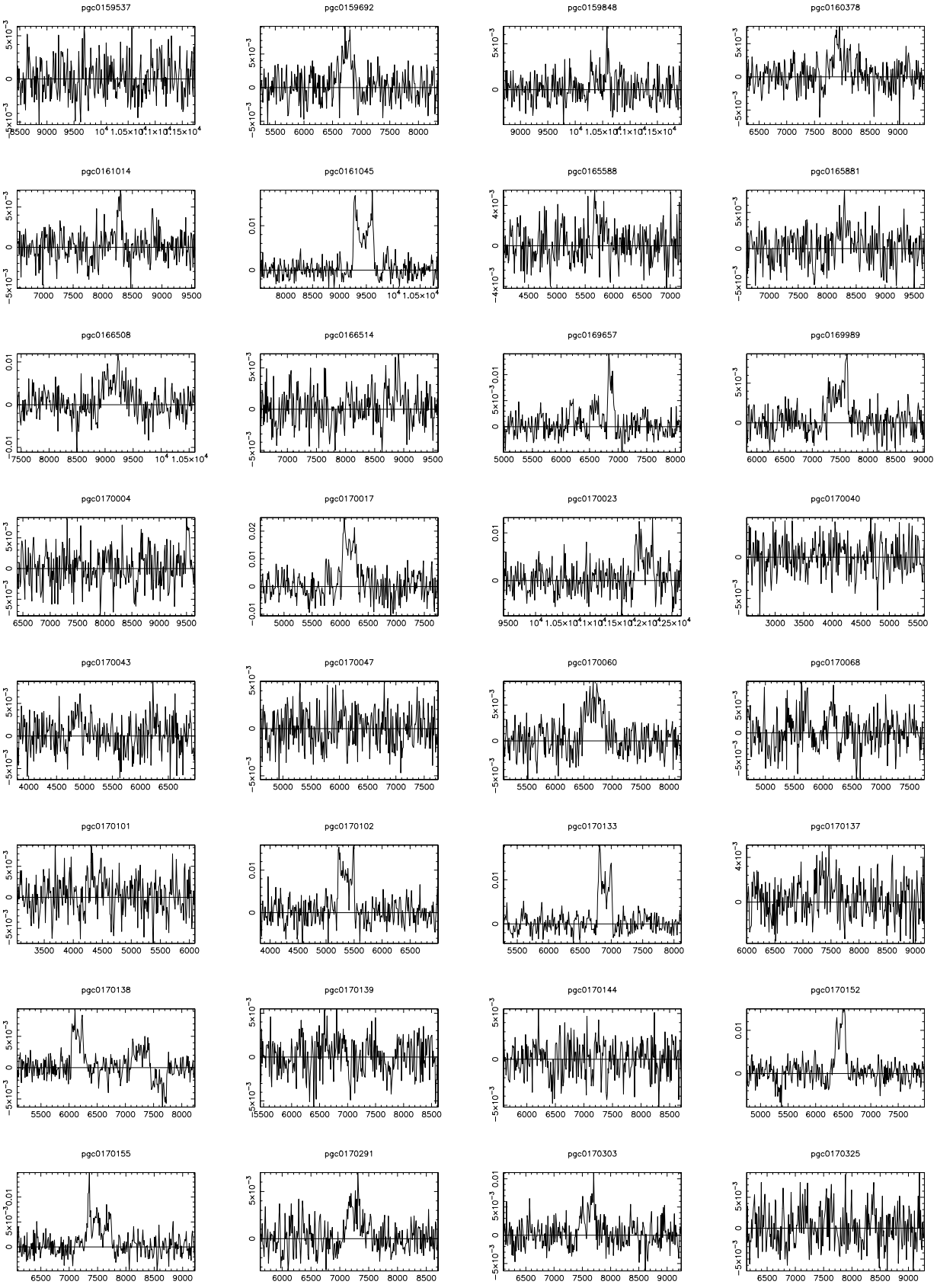

Fig. A.1. Fig. 2 **v.** HI profiles. Continued.

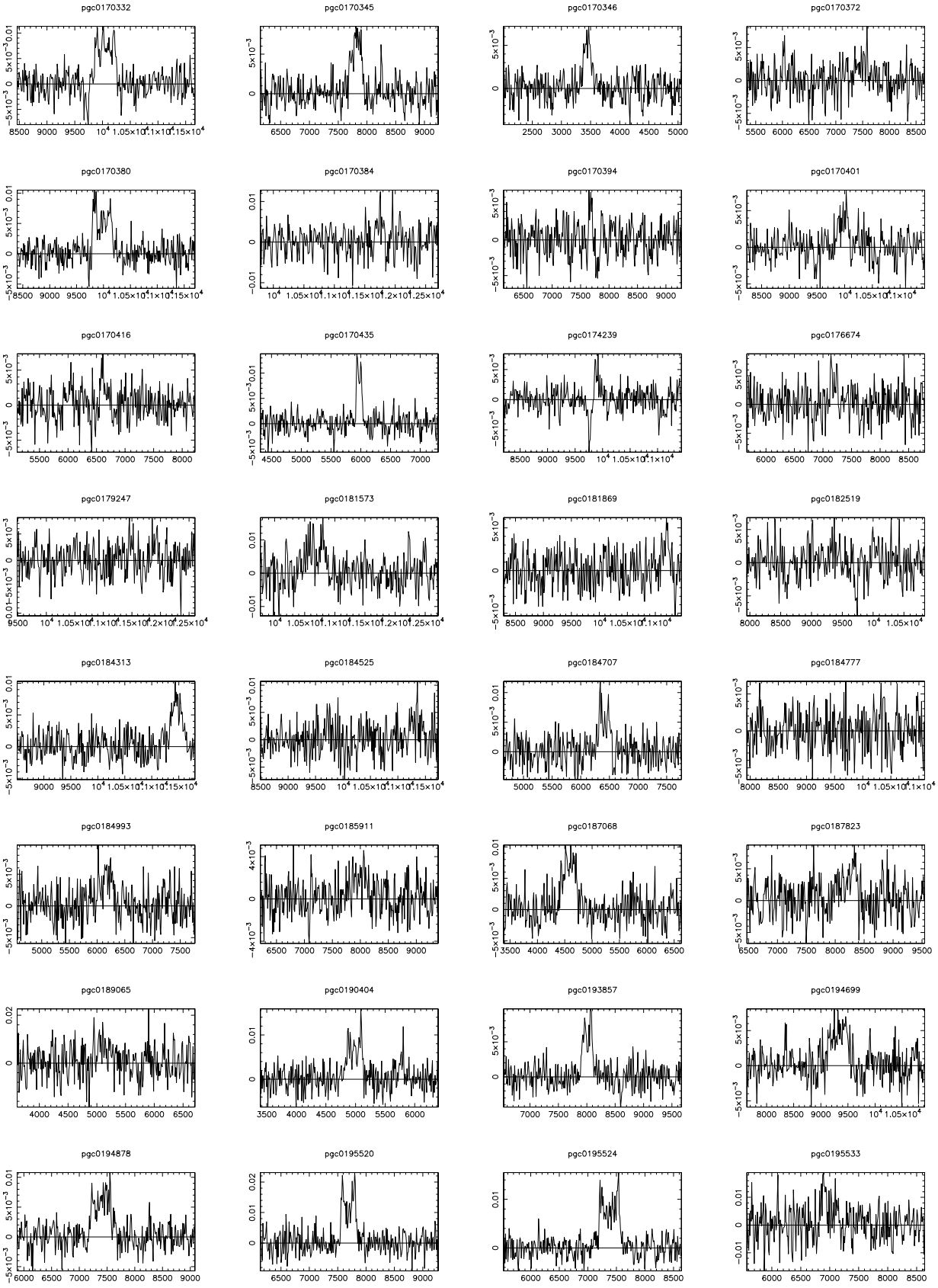

Fig. A.1. Fig. 2 **w.** HI profiles. Continued.

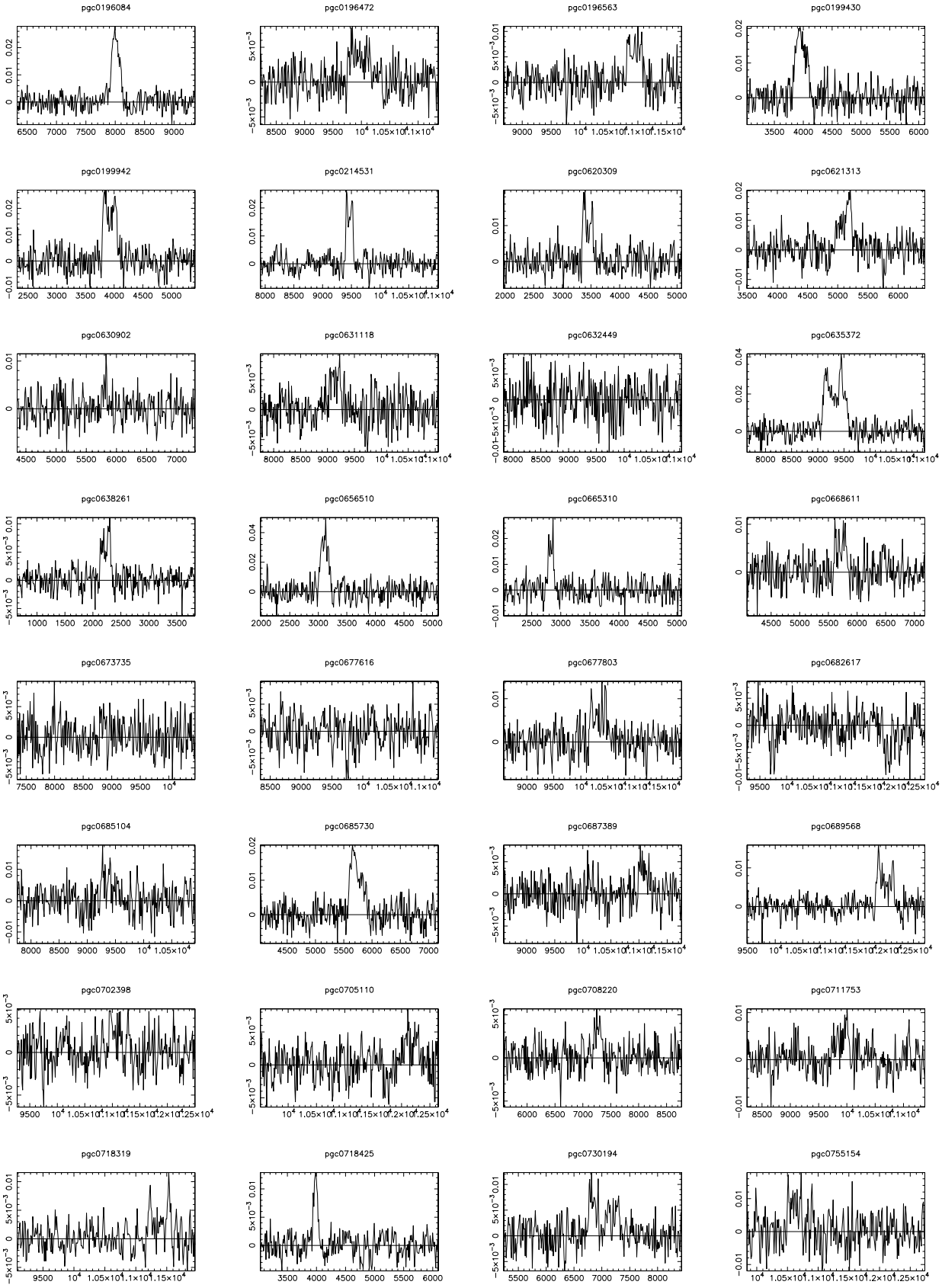

Fig. A.1. Fig. 2 **x.** HI profiles. Continued.

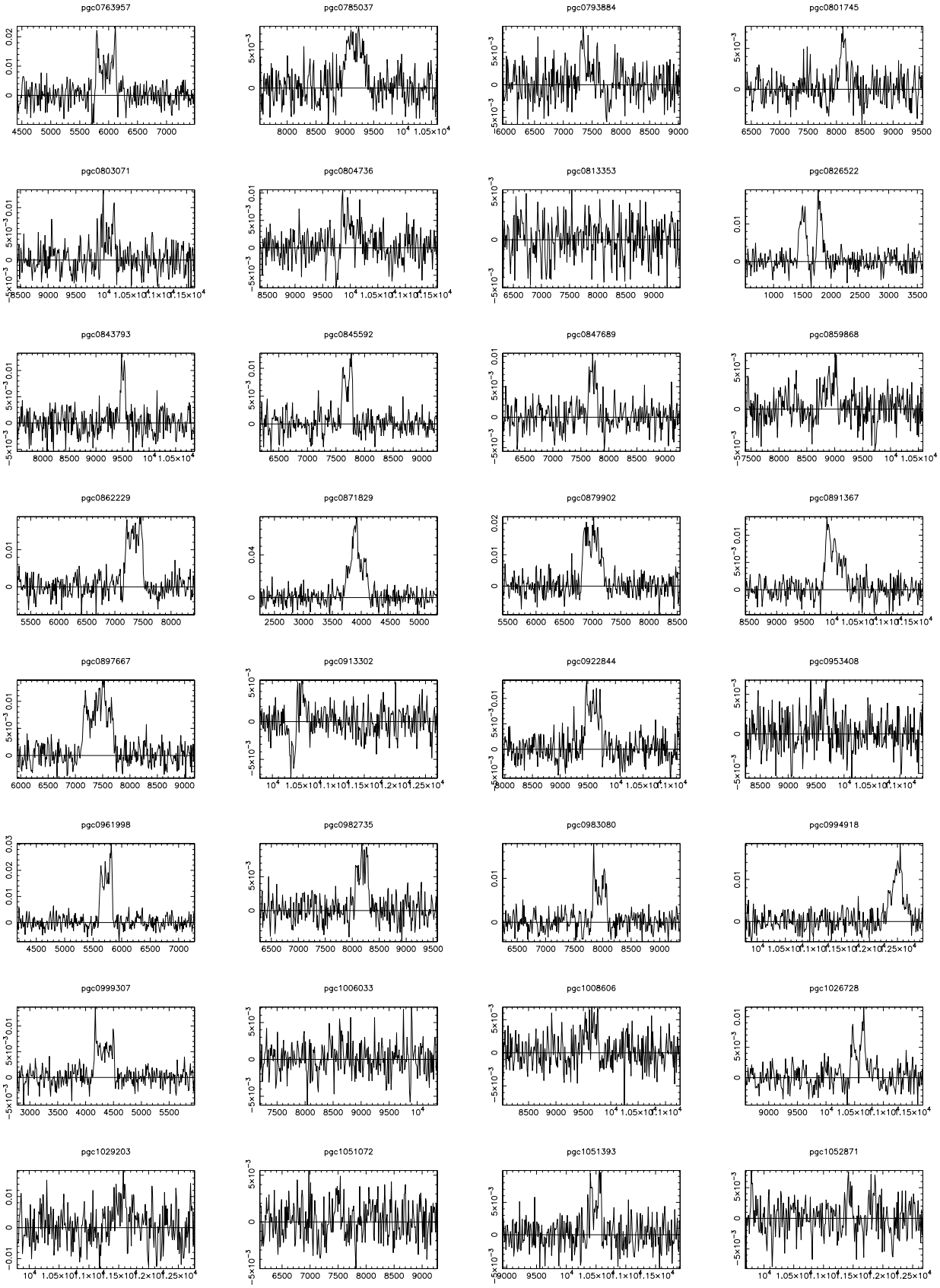

Fig. A.1. Fig. 2 **y.** HI profiles. Continued.

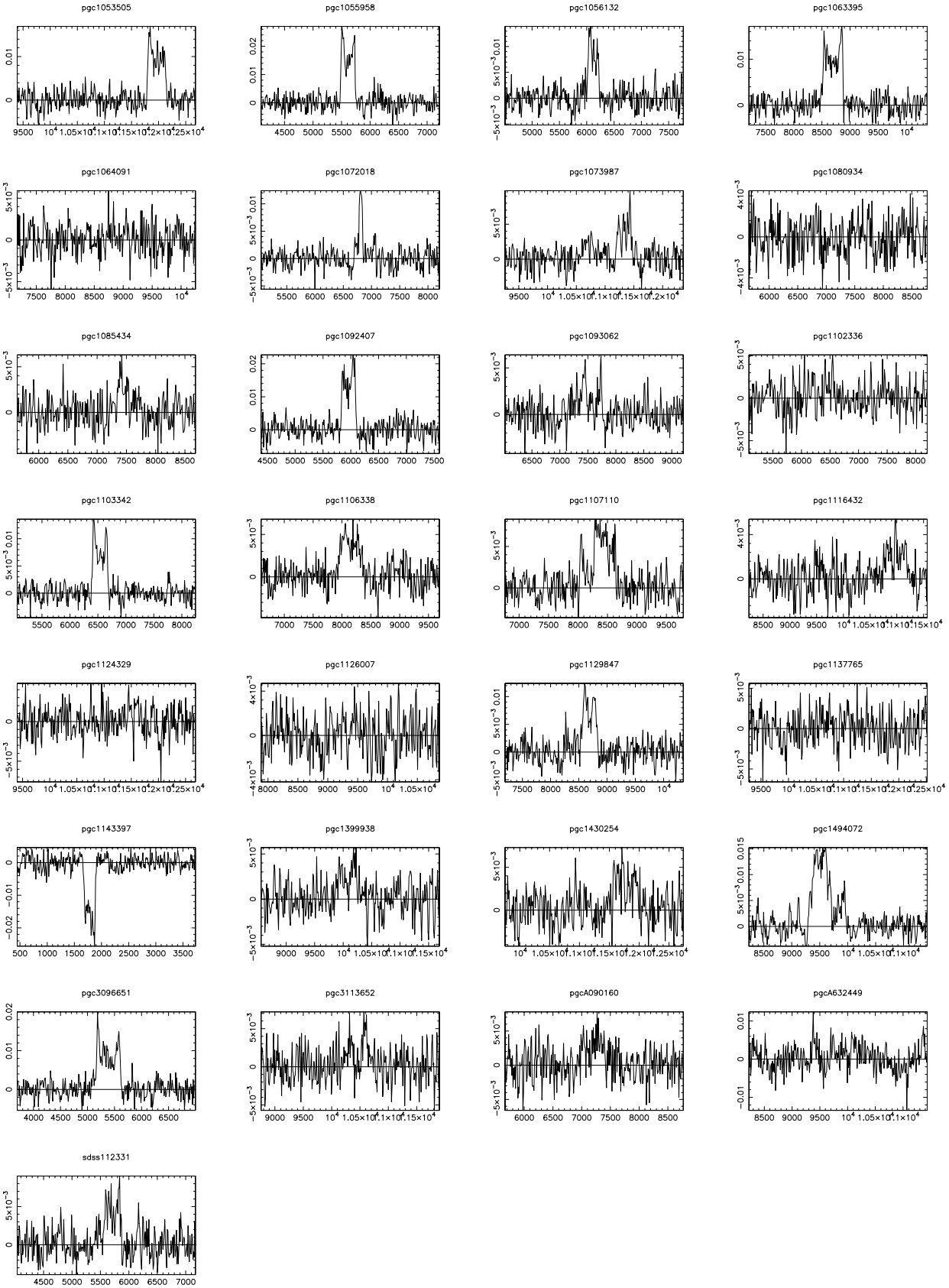

Fig. A.1. Fig. 2 **z.** HI profiles. Continued.